

2

NONPLANAR METHOD FOR PREDICTING INCOMPRESSIBLE
AERODYNAMIC COEFFICIENTS OF RECTANGULAR
WINGS WITH CIRCULAR-ARC CAMBER

By

John Everett Lamar

B.S. in Aerospace Engineering

B.S. in Mechanical Engineering

M.S. in Aerospace Engineering

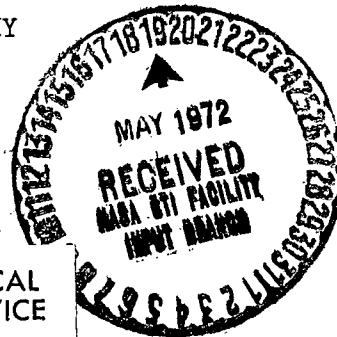
Thesis submitted to the Graduate Faculty of the
Virginia Polytechnic Institute and State University
in candidacy for the degree of

DOCTOR OF PHILOSOPHY

in

Aerospace Engineering

Reproduced by
NATIONAL TECHNICAL
INFORMATION SERVICE
U S Department of Commerce
Springfield VA 22151



December 1971

(NASA-TM-X-67791) NONPLANAR METHOD FOR
PREDICTING INCOMPRESSIBLE AERODYNAMIC
COEFFICIENTS OF RECTANGULAR WINGS WITH
CIRCULAR-ARC CAMBER Ph.D. Thesis - J.E.
Lamar (NASA) Dec. 1971 94 p

N72-22995

Unclas
27278

CSCL G1A G3/C1

NONPLANAR METHOD FOR PREDICTING INCOMPRESSIBLE
AERODYNAMIC COEFFICIENTS OF RECTANGULAR
WINGS WITH CIRCULAR-ARC CAMBER

by

John Everett Lamar

Thesis submitted to the Graduate Faculty of the
Virginia Polytechnic Institute and State University
in partial fulfillment of the requirements for the degree of

DOCTOR OF PHILOSOPHY

in

Aerospace Engineering

APPROVED:

Joseph A. Schetz

Dr. Joseph A. Schetz

Daniel Frederick

Dr. Daniel Frederick

Fred R. DeJarnette

Dr. Fred R. DeJarnette

J. C. Smith

Dr. J. C. Smith

C. D. Williams

Dr. C. D. Williams

December 1971

Blacksburg, Virginia

NONPLANAR METHOD FOR PREDICTING INCOMPRESSIBLE
AERODYNAMIC COEFFICIENTS OF RECTANGULAR
WINGS WITH CIRCULAR-ARC CAMBER

By

John Everett Lamar

B.S. in Aerospace Engineering

B.S. in Mechanical Engineering

M.S. in Aerospace Engineering

Thesis submitted to the Graduate Faculty of the
Virginia Polytechnic Institute and State University
in candidacy for the degree of

DOCTOR OF PHILOSOPHY

in

Aerospace Engineering

December 1971

NONPLANAR METHOD FOR PREDICTING INCOMPRESSIBLE
AERODYNAMIC COEFFICIENTS OF RECTANGULAR
WINGS WITH CIRCULAR-ARC CAMBER

By

John Everett Lamar

B.S. in Aerospace Engineering

B.S. in Mechanical Engineering

M.S. in Aerospace Engineering

Thesis submitted to the Graduate Faculty of the
Virginia Polytechnic Institute and State University
in candidacy for the degree of

DOCTOR OF PHILOSOPHY

in

Aerospace Engineering

December 1971

Blacksburg, Virginia

NONPLANAR METHOD FOR PREDICTING INCOMPRESSIBLE
AERODYNAMIC COEFFICIENTS OF RECTANGULAR
WINGS WITH CIRCULAR-ARC CAMBER

By

John Everett Lamar

ABSTRACT

The development of a nonplanar lifting surface method having a continuous distribution of singularities and satisfying the tangent flow boundary condition on the mean camber surface is given in this dissertation. The method predicts some incompressible longitudinal aerodynamic coefficients of rectangular wings which have circular-arc camber. The solution method is of the integral-equation type and the resulting surface integrals are evaluated by either using numerical or analytical techniques, as are appropriate.

Applications of this method are made and the results compared with those from an exact two-dimensional circular-arc camber solution, a three-dimensional flat-wing solution which represents the camber by a projected slope onto the flat surface, and a flat-wing experiment. From these comparisons, the present method is found to predict well the flat-wing experiment and limiting values, in addition to the center of pressure variation at an angle of attack of zero for any camber. For wings having camber ratios larger than about 1.25% and moderate to high aspect ratios, the results of the present method deteriorate due to the inadequacy of lifting pressure modes employed.

II. TABLE OF CONTENTS

CHAPTER		PAGE
I.	TITLE	i
II.	TABLE OF CONTENTS	ii
III.	ACKNOWLEDGEMENTS.	iv
IV.	LIST OF SKETCHES, FIGURES, AND TABLES	v
V.	LIST OF SYMBOLS	viii
VI.	INTRODUCTION.	1
VII.	THEORETICAL DEVELOPMENT	7
	Basic Formulation	7
	Concepts.	7
	First Level Integrations.	17
	Pressure Functions.	19
	Final Form of Integral Equation	22
	General Surface Integrations.	23
	Surface Integrations Over the Control-Point Box	24
	Expansions.	25
	Approximate Forms	25
	Integrated Results.	27
	Surface Integrations Over the Image-Point Box	29
	Solution Technique.	30
VIII.	RESULTS AND DISCUSSION.	32
	General	32
	Variation of Results With -	
	Box Size.	33

CHAPTER	PAGE
Spanwise Control Point Locations	34
Chordwise Control Point Locations	35
Number of Chordal Control Points	36
Experimental Data Comparison	38
Theoretical Comparisons.	41
Two- and Three-Dimensional Lifting Pressures . .	41
Two-Dimensional Cambered Wings	41
Over an Aspect Ratio Range	46
Over a Camber Ratio Range.	49
Over an Angle-of-Attack Range.	51
Discussion	51
IX. CONCLUSIONS	55
X. RECOMMENDATIONS	57
XI. REFERENCES	58
XII. VITA	61
XIII. APPENDIX A: Certain Integrals Over the Box	62
XIV. APPENDIX B: Determination of Aerodynamic	
Coefficients	65
XV. APPENDIX C: Two-Dimensional Circular-Arc Airfoil	
Aerodynamic Characteristics.	68

III. ACKNOWLEDGEMENTS

The author would like to express his appreciation to the following people:

At the NASA - Langley Research Center:

1. Mr. P. J. Bobbitt for his patience, encouragement, and insight into the problem undertaken;
2. Mr. E. C. Polhamus for discussions regarding data presentation; and
3. Mrs. John Ambrose for her help in typing parts of this dissertation.

Elsewhere:

1. Dr. F. R. DeJarnette, currently of the Mechanical and Aerospace Engineering Department of North Carolina State University, for serving as my committee chairman and for his continuing interest in the dissertation topic; and
2. my wife for typing a major portion of this dissertation.

IV. LIST OF SKETCHES, FIGURES, AND TABLES

SKETCH	PAGE
1. Camber representation in flat-wing solution	4
2. Representation of a rectangular wing having a constant circular-arc camber.	5
3. Velocity diagram on the surface of a circular-arc section at R, ϑ	10
(a) Upper surface.	10
(b) Lower surface.	10
4. Path of first level of integration.	12
5. Distance between point on pressure doublet sheet and a point on the path of integration.	16
6. Loading mode shapes	20
7. Relationship between ϵ and ϑ	21
8. Integration regions and number of integration points used in each for low-to-moderate camber.	23
9. Loading composition for finite-aspect ratio flat and cambered wings.	48
10. Geometrical relationships between generating circle and circular-arc airfoil	68
11. Additional geometrical relationships between generating circle and circular-arc airfoil. . .	69

1. Lifting pressure coefficient distribution for
 $A = 4$ flat rectangular wing at $2y/b = 0$
and $\alpha = 4.35^\circ$ 40
2. Lifting pressure coefficient distribution for
three-dimensional methods at $A = 20$ and
 $2y/b = 0$ and two-dimensional exact method,
all at $\alpha = 5^\circ$
 - (a) $h/c = .00125$ 42
 - (b) $h/c = .0314$ 43
3. Two-dimensional lifting pressure coefficient
distribution for $h/c = .5$ at $\alpha = 5^\circ$ 45
4. Effect of camber on center of pressure.
Cambered wing results are at $\alpha = 0^\circ$ 47
5. Effect of camber on some aerodynamic character-
istics of an $A = 5$ rectangular wing at
 $\alpha = 5^\circ$
 - (a) x_{cp} 50
 - (b) C_L 50
6. Effect of angle of attack on C_L for an $A = 5$,
 $h/c = .0314$ rectangular wing. 52

I	Number of Integration Stations Required for Different Box Sizes and Effect of Box Size on Aerodynamic Characteristics for an $A = 20$, $h/c = .00125$ Rectangular Wing at $\alpha = 5^\circ$. Control Points at $x/c = .345, .905$	34
II	Effect of Spanwise Location of Control Point Rows on Aerodynamic Characteristics of an $A = 20$, $h/c = .00125$ Rectangular Wing at $\alpha = 5^\circ$. Control Points at $x/c = .345, .905$	34
III	Effect of Locating Two Control Points on the Aerodynamic Characteristics of an $A = 5$, $h/c = .00125$ Rectangular Wing at $\alpha = 5^\circ$. . .	36
IV	Effect of Number and Locations of Control Points on the Aerodynamic Characteristics of an $A = 5$, $h/c = 0.0314$ Rectangular Wing at $\alpha = 5^\circ$. . .	37
V	Experimental and Theoretical Aerodynamic Characteristics for an $A = 4$ Flat Rectangular Wing	39
VI	Circular-Arc Lift and Center of Pressure	44

V. LIST OF SYMBOLS

A	aspect ratio
[A]	aerodynamic influence coefficient matrix
a	radius of circle used to generate circular arc section
B	see equation (33c)
b	wing span
C	see equation (33d)
C_D	drag coefficient, $\frac{\text{Drag}}{q S}$
C_L	lift coefficient, $\frac{\text{Lift}}{q S}$
C_m	pitching-moment coefficient, $\frac{\text{Moment}}{q S c_{ref}}$
C_s	suction coefficient, $\frac{\text{Suction}}{q S}$
c	chord
c_{av}	average chord
c_{d_c}	section camber drag coefficient
c_l	section lift coefficient
c_m	section pitching-moment coefficient
c_{nm}	coefficient of the n^{th} chordwise and m^{th} spanwise pressure mode shape
c_s	section suction coefficient
c_x	local x force coefficient in complex plane
c_y	local y force coefficient in complex plane
D	see equation (33b)
h	maximum camber height above chord plane
h_n	n^{th} chordwise pressure mode, (see equation (35))
i	$\sqrt{-1}$

k	$c/4$
LE	leading edge
M	pitching moment - three-dimensional result in main text; two-dimensional result in appendix C
N	normal force, number of lifting pressure functions used
n	normal direction
P_1	see equation (C-23a)
P_2	see equation (C-23b)
p	see equation (31)
q	free-stream dynamic pressure, $1/2\rho V^2$
\bar{R}, θ, y	location of control point
R', θ', y	location of dummy point on path of integration
R^*, δ, y_1	location of point of pressure doublet sheet
R	radius of circular-arc section
$R()$	real part of ()
r	radius, distance between point on pressure doublet sheet and control point; see equations (29a) and (33a)
S	area
s	complex coordinate location of center of generating circle
TE	trailing edge
u, v	velocity components in the complex plane in the x and iy directions, respectively
$u(x, y, z)$	perturbation velocity in the free-stream direction
\bar{u}_n	perturbation normal velocity
\bar{u}_t	perturbation tangential velocity
V	free-stream velocity, volume

w	complex potential
X, Y	forces in the complex plane in the x and iy directions, respectively
X, Y, Z	cartesian axes in three-dimensional solution
x, iy	complex coordinates in z plane
x, y, z	distances along the x, y, z axes
x_1, y_1, z_1	coordinates of a point on the pressure doublet sheet
x'	dummy variable along the x axis; also, distance along chord
x_{cp}	fractional chordwise location of center of pressure, aft of leading edge
z	complex variable in circular-arc plane, $x + iy$; also, constant during θ' integration, see equation (17)
α	angle of attack, degrees
α_i	induced angle of attack
β	$\angle CH_1A$, see sketch 10
$\bar{\beta}$	$\beta - \alpha$
γ	angular coordinate of a point on generating circle, see sketch 11
γ_c	circulation distribution on a circular arc section
$\Delta C_p(\vartheta, y_1)$	lifting pressure coefficient over the wing
$\Delta C_p(\epsilon, y_1)$	see equation (35a)
$\Delta p(\vartheta, y_1)$	lifting pressure over the wing
ϵ	angle used in describing chordwise pressure mode shapes
ϵ_θ	ϵ which corresponds to the same longitudinal location as for $\vartheta = \theta$
ζ	complex variable in circle plane, $\xi + i\eta$

η	non-dimensional spanwise variable, $2y_1/b$
θ_o	angular location of the leading edge in polar coordinates
θ_1	angular location of the trailing edge in polar coordinates
ξ, η	complex coordinates in ζ plane
ρ	density
σ, ω	perturbation angular and lateral variables in camber and spanwise directions, respectively
$\bar{\sigma}, \bar{\omega}$	maximum values of σ and ω , respectively (note that in this analysis $R\bar{\sigma} = \bar{\omega}$)
$\phi(x,y,z), \phi(R',\theta,y)$	perturbation velocity potential
ω_R	see equation (C-23c)
ω_I	see equation (C-23d)

Subscripts:

c	center of circle used to generate circular arc section, camber
F	focal point
H	trailing-edge point on the circular arc airfoil
i, ii	induced — far field, near field
LE	leading edge
l	lower surface
lo	lower limit
ref	reference
u	upper surface
up	upper limit
w	wake

VI. INTRODUCTION

Solutions for the steady aerodynamic characteristics of wings began with Prandtl (ref. 1) and his famous "lifting line" concept. In this concept, the loading was concentrated along a straight line and all induced effects on the wing came from the trailing vortex sheet. The local effective angles of attack were composed of the geometric angles and the induced angles along the lifting line. This concept was useful in predicting the characteristics of lifting systems employing rectangular wings of high aspect ratio by representing the span loading as either an averaged constant value or a semi-elliptical variation. However, as the planforms became more complex, additional improvements in the theory were necessary in order to predict the aerodynamic characteristics. The improvements can be classified in three ways: (1) extension of Prandtl's concept to other planforms, (2) inclusion of the induced-camber effects in the lift distribution, and (3) allowance for nonplanar lifting systems (other than biplanar).

Prandtl's "lifting line" method and the extensions employed to allow for the consideration of other than rectangular planforms provided span load distribution, and in some instances, determined the induced drag as well. For instance, Multhopp (ref. 2) devised a method for determining the span load distribution on any wing that could be represented by a straight lifting line. Mutterperl (ref. 3) developed a method for determining span loading on sweptback wings by using a bound vortex (that is, a lifting line of variable strength) lying along the quarter chord of each wing panel, as well as a sheet of trailing vorticity.

The strengths of the vortex system were constrained to give tangent flow on the wing three-quarter chord line. This relationship between the bound-vortex position and the tangent-flow-boundary line is the same as for the two-dimensional solution, which is one that develops the correct lift value. Weissinger (ref. 4) developed both lifting-surface and lifting-line methods for sweptback wings, and used the tangent flow constraint at the three-quarter-chord location to obtain solutions.

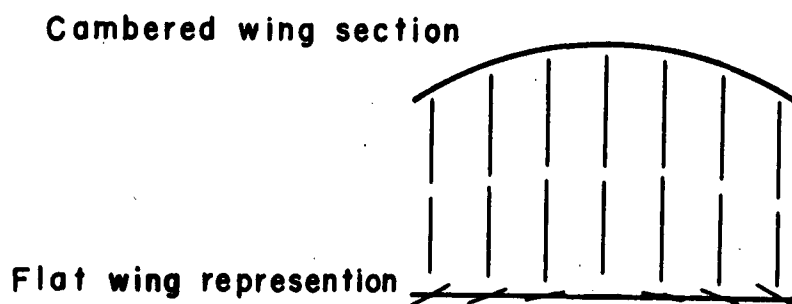
The inclusion of the induced-camber effects on three-dimensional planar wings is seen in two important ways. One is the removal of the constraint that the section center of pressure be at the quarter chord, and the other is the improvement in predicting the lifting-pressure (difference between lower and upper surface pressures) distribution because of the increased amount of information. All of this is accomplished by either expanding the number of chordwise mode shapes or placing additional bound-vortex elements and control points along the chord, or, as Faulkner (ref. 5) did, with a combination of the two. The lifting surface method of Faulkner's is called "vortex lattice theory" and is based on representing the induced effects of the lifting system by using a lattice of horseshoe vortices, the strengths of which are determined by a series of modal functions. In this solution, there would be as many coefficients in the series as control points (points at which the tangent flow boundary conditions are satisfied), but not as many as there are horseshoe vortices. Also, Multhopp (ref. 6) developed a lifting surface method called "subsonic

lifting surface theory" which used two modes of pressure chordwise and two control points at several spanwise stations and could be applied to arbitrary planforms.

Since reference 6, there have been many other lifting surface methods published for steady subsonic flow. Each new method, in general, begins with an already-developed fundamental method and seeks to improve its accuracy by (1) adding additional chordwise loading terms (refs. 7 and 8), (2) reformulating the solution (ref. 9), (3) performing the integrations differently (ref. 10), or (4) extending the original concepts. For example, extensions to Faulkner's work can be made easily by requiring that the distribution of vortex strengths be individually determined (not expressed in a series) by a solution to a set of linear simultaneous equations employing as many control points as unknown vortex strengths. (See, for example, references 11, 12, and 13.) Many of the latter-referenced methods would not have been practical to use before the advent of the high-speed digital computer.

Solutions for nonplanar lifting surfaces, such as wings with dihedral, have been made with the vortex-lattice method (refs. 11 and 14), kernel-function-integral equation (ref. 15), and an asymptotic-expansion procedure (ref. 16). Other nonplanar solutions are available for intersecting tail surfaces, among them references 11, 17, and 18. In each solution, the boundary conditions are satisfied on the chordal plane. However, for wings which are nonplanar in the chordwise direction (that is, for a cambered wing), simplifying

assumptions are usually made in order to effect a solution. The major assumption is that of satisfying the boundary conditions of the cambered wing on a lifting surface lying in a plane formed by the longitudinal and spanwise variables of a wind axis system by projecting the wing slopes onto the plane. (See sketch 1 and, for example solutions, see references 8 and 14.)

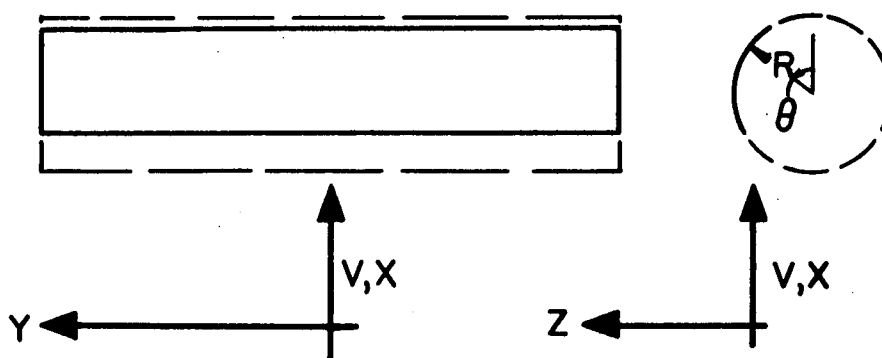


Sketch 1. Camber representation in flat-wing solution.

By doing this, the effect of the vertical displacements between influencing and influenced points is not taken into account. Another method (ref. 19), which satisfies the boundary conditions on the surface of the cambered wing, does not satisfy the Kutta condition at the trailing edge because the solution is based upon solving a series of two-dimensional cross-flow problems. The formulation of the vortex-lattice method, as given in reference 11, appears to be general enough to account for vertical displacements as well as to satisfy the boundary conditions on the surface. However, constraints would have to be imposed in order to guarantee that the trailing vortex system only exited the wing at the trailing edge.

In consideration of the limitations of the methods just dis-

cussed, it seems appropriate to develop a solution for the cambered wing problem which would (1) satisfy the boundary conditions on the surface, (2) account for the vertical displacements between influencing and influenced points, and (3) satisfy the Kutta condition at the trailing edge. This dissertation describes such a solution for rectangular wings having circular-arc camber (see sketch 2).



Sketch 2. Representation of a rectangular wing having a constant circular-arc camber.

The solution developed herein uses a more general form of the subsonic integral equation than the methods discussed for planar wings, because it must relate the normal component of perturbation velocity - rather than the downwash - to the lifting pressure, and it must include the effects of vertical displacement. Furthermore, the present method of solution employs both numerical and analytical techniques. The latter are applied in a small region (square box in the surface) surrounding the control point, because it is at the control point that the integral equation has a singularity. This technique encompasses expansions in small parameters, followed by analytic integrations over the box. Outside of the box, the integral equation is evaluated numerically.

Results obtained with the present method are compared with both an exact two-dimensional circular-arc-camber solution and a three-dimensional flat lifting surface which employs the slope-projection procedure to account for camber. Due to the general unavailability of experimental data for circular-arc-cambered wings, comparisons with experiment are only made for flat wings. From the comparisons made, conclusions are drawn about the applicability of the present method over the camber- and aspect-ratio and angle of attack ranges. In addition to these applications, the present method may be extended to certain wing-flap systems that approximate the circular-arc-camber constraint.

Three appendices are given: appendix A discusses some of the integral types which must be integrated over the box surrounding the control point; appendix B presents the equations used to compute some section and wing aerodynamic coefficients; and appendix C gives the development of the aerodynamic characteristics of the two-dimensional circular-arc airfoil, included herein for completeness.

VII. THEORETICAL DEVELOPMENT

Basic Formulation

Concepts

The method of solution for pressure loading over a wing having circular-arc mean camber line (sketch 2) will begin with Poisson's equation (see ref. 20), as does the flat-wing solution. The basic concept here is that the general perturbation velocity field will be the same for both wings, with differences occurring primarily in the vicinity of and aft of the wing. It is possible, therefore, to make use of some of the solution techniques which have been developed for the flat wing in seeking a solution to this problem.

From reference 20, the three-dimensional Poisson's equation can be written for the perturbation velocity in the freestream direction as

$$u(x,y,z) = -\frac{1}{4\pi} \iiint_V \frac{1}{r} \nabla^2 u dV + \frac{1}{4\pi} \iint_S \left[u \frac{\partial}{\partial n} \left(\frac{1}{r} \right) - \frac{1}{r} \frac{\partial u}{\partial n} \right] dS \quad (1)$$

By representing the wing surface with a sheet of pressure doublets, the perturbation velocity can be related to a velocity potential. The velocity potential due to each pressure doublet is of the form

$\frac{-(z-z_1)}{r^3}$ and is a solution of Laplace's equation

$$\nabla^2 \phi(x,y,z) = 0 \quad (2)$$

Upon relating $u(x,y,z)$ to ϕ by

$$u(x,y,z) = \phi_x \quad (3)$$

substituting equation (3) into equation (2), and interchanging orders or differentiation, it follows that

$$\nabla^2 u = 0 \quad (4)$$

Hence,

$$u(x,y,z) = \frac{1}{4\pi} \int \int_S \left[u \frac{\partial}{\partial n} \left(\frac{1}{r} \right) - \frac{1}{r} \frac{\partial u}{\partial n} \right] dS \quad (5)$$

The surface S includes both the upper and lower surfaces of the wing, as well as the wake upper and lower surface area. Since the flow is assumed to remain attached to the wing, only leaving at the trailing edge and thereby satisfying the Kutta condition, the perturbation velocity in the freestream direction on either side of the wake surface must be the same. Consequently, the lifting pressure is zero. Hence, upon examining the wake portion of equation (5),

$$\iint_{S_{wu}} \left[u_u \frac{\partial}{\partial n} \left(\frac{1}{r} \right) - \frac{1}{r} \frac{\partial u_u}{\partial n} \right] dS + \iint_{S_{wl}} \left[u_l \frac{\partial}{\partial n} \left(\frac{1}{r} \right) - \frac{1}{r} \frac{\partial u_l}{\partial n} \right] dS ,$$

it can be seen that, since $u_u = u_l$ and $\frac{\partial}{\partial n} \left(\frac{1}{r} \right)$ on the upper surface is opposite to the same term on the lower surface, the first terms in each integral cancel. That is,

$$\int \int_{S_{wu}} \left[u_u - u_l \right] \frac{\partial}{\partial n} \left(\frac{1}{r} \right) dS = 0 \quad (6)$$

Also, for wake shapes that are straight or circular arc, the normal derivatives of u are continuous across the wake because they are related to the continuous streamwise derivatives of the normal velocity components through irrotationality. This leads to cancellation of the second terms in each integral. That is,

$$\iint_{S_{w_u}} \left[-\frac{1}{r} \frac{\partial u_u}{\partial n} \right] dS + \iint_{S_{w_l}} \left[-\frac{1}{r} \frac{\partial u_l}{\partial n} \right] dS = 0 \quad (7)$$

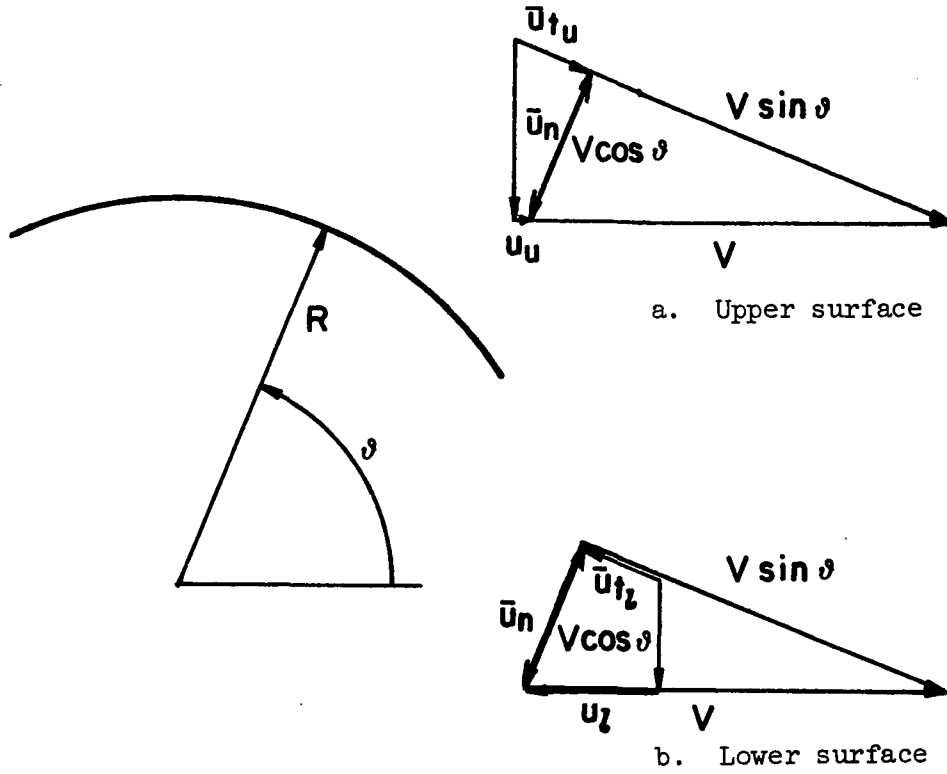
Thus, the integral equation that remains to be evaluated is

$$u(x,y,z) = \frac{1}{4\pi} \left\{ \iint_{S_u} \left[u_u \frac{\partial}{\partial n} \left(\frac{1}{r} \right) - \frac{1}{r} \frac{\partial u_u}{\partial n} \right] dS + \iint_{S_l} \left[u_l \frac{\partial}{\partial n} \left(\frac{1}{r} \right) - \frac{1}{r} \frac{\partial u_l}{\partial n} \right] dS \right\} \quad (8)$$

The coordinate system chosen in which to solve this equation is cylindrical polar because of the ease in applying the boundary conditions. In this system, the mean camber surface lies on a surface of constant radius. Hence, the normal direction is along a radius vector R^* , the tangential direction is along ϕ , and the spanwise direction is along y_1 . This leads to

$$u(x,y,z) = \frac{1}{4\pi} \iint_S \left[[u_u - u_l] \frac{\partial}{\partial R^*} \left(\frac{1}{r} \right) \Big|_{R^*=R} - \left(\frac{1}{r} \right) \Big|_{R^*=R} \left(\frac{\partial u_u}{\partial R^*} - \frac{\partial u_l}{\partial R^*} \right) \Big|_{R^*=R} \right] dS \quad (9)$$

From sketch 3,



Sketch 3. Velocity diagram on the surface
of a circular-arc section at R, θ

it can be seen that

$$u_u = \bar{u}_{t_u} \sin \theta - \bar{u}_n \cos \theta \quad (10a)$$

and

$$u_l = \bar{u}_{t_l} \sin \theta - \bar{u}_n \cos \theta \quad (10b)$$

By differentiating equations (10a) and (10b) with respect to R^* , the following equations are obtained:

$$\frac{\partial u_u}{\partial R^*} = \sin \theta \frac{\partial \bar{u}_{t_u}}{\partial R^*} - \cos \theta \frac{\partial \bar{u}_n}{\partial R^*} \quad (11a)$$

and

$$\frac{\partial u_1}{\partial R^*} = \sin \vartheta \frac{\partial \bar{u}_{t_1}}{\partial R^*} - \cos \vartheta \frac{\partial \bar{u}_n}{\partial R^*} \quad (11b)$$

with \bar{u}_n being continuous across the plane of the wing, or along R^* .

The irrotationality condition, when written in cylindrical-polar coordinates, gives the needed relationships between the perturbation velocities tangent and normal to the camber surface as

$$\frac{\partial \bar{u}_{t_u}}{\partial R^*} = -\frac{1}{R^*} \frac{\partial \bar{u}_n}{\partial \vartheta} - \frac{\bar{u}_{t_u}}{R^*} \quad (12a)$$

and

$$\frac{\partial \bar{u}_{t_1}}{\partial R^*} = -\frac{1}{R^*} \frac{\partial \bar{u}_n}{\partial \vartheta} - \frac{\bar{u}_{t_1}}{R^*} \quad (12b)$$

Therefore, when the results of equations (11a), (11b), (12a), and (12b) are substituted into equation (9), the result is

$$u(x,y,z) = \frac{1}{4\pi} \iint_S \left[(\bar{u}_{t_u} - \bar{u}_{t_1}) \sin \vartheta \frac{\partial}{\partial R^*} \left(\frac{1}{r} \right) \right]_{R^*=R} - \sin \vartheta \left(-\frac{\bar{u}_{t_u} + \bar{u}_{t_1}}{rR^*} \right)_{R^*=R} \right] dS \quad (13)$$

Let

$$\gamma_c \equiv (\bar{u}_{t_u} - \bar{u}_{t_1}) \quad (14a)$$

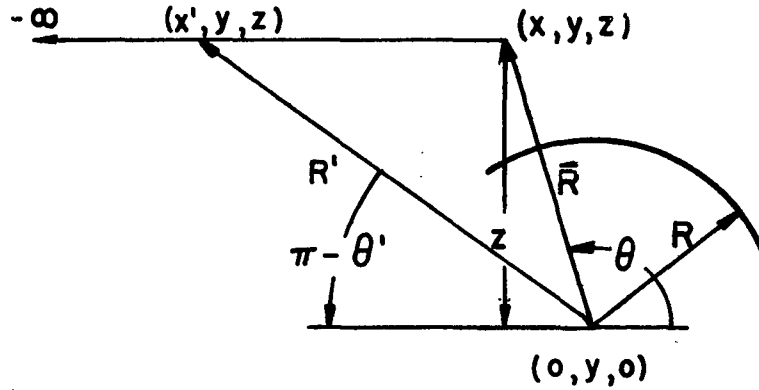
Then

$$u(x,y,z) = \frac{1}{4\pi} \iint_S \gamma_c \sin \vartheta \left[\left. \frac{\partial}{\partial R^*} \left(\frac{1}{r} \right) \right|_{R^*=R} + \left(\frac{1}{R^* r} \right) \right|_{R^*=R} \right] dS \quad (14b)$$

The velocity potential associated with this perturbation velocity can be determined by

$$\phi(x,y,z) = \int_{-\infty}^x u(x',y,z) dx' \quad (15)$$

The minus infinity value is chosen as the lower limit because there the velocity potential is zero.



Sketch 4. Path of first level of integration.

From sketch 4 it can be seen that

$$x' = R' \cos \theta' \quad (16a)$$

and hence

$$dx' = dR' \cos \theta' + R' (-\sin \theta' d\theta') \quad (16b)$$

The x' integration must take place at a constant z elevation, as in the flat-wing solution; therefore, by setting

$$z = R' \sin\theta' = \bar{R} \sin\theta \quad (17)$$

equation (16b) can be re-expressed in terms of the constant z as

$$dx' = d(z/\sin\theta') \cos\theta' - z d\theta' \quad (18)$$

Since

$$dR' = \frac{dR'}{d\theta'} (d\theta') = \frac{d(z/\sin\theta')}{d\theta'} (d\theta') = \frac{-z \cos\theta'}{\sin^2\theta'} (d\theta') \quad (19)$$

then

$$dx' = \frac{-z \cos^2\theta'}{\sin^2\theta'} (d\theta') - z d\theta' = \frac{-z d\theta'}{\sin^2\theta'} \quad (20)$$

or

$$dx' = \frac{-R' d\theta'}{\sin\theta'} = \frac{-\bar{R} \sin\theta d\theta'}{\sin^2\theta'} \quad (21)$$

and the limits of integration go from π to θ . Therefore,

$$\phi(\bar{R}, \theta, y) = \frac{1}{4\pi} \int_{\pi}^{\theta} \int_S \gamma_c \sin\theta \left[\frac{\partial}{\partial R^*} \left(\frac{1}{r} \right) \right]_{R^*=R} + \left(\frac{1}{R^* r} \right) \Big|_{R^*=R} dS \left(\frac{-\bar{R} d\theta'}{\sin^2\theta'} \right) \sin\theta \quad (22)$$

Once the velocity potential is known, differentiation with respect to \bar{R} will yield the perturbation normal velocity. Hence

$$\bar{u}_n(\bar{R}, \theta, y) = \frac{\partial \phi(\bar{R}, \theta, y)}{\partial \bar{R}} \quad (23a)$$

and so

$$\bar{u}_n(\bar{R}, \theta, y) = \frac{1}{4\pi} \iint_S \int_{\pi}^{\theta} \frac{\partial}{\partial \bar{R}} \left\{ \frac{-\gamma_c \sin^3 \bar{R} \sin \theta}{\sin^2 \theta'} \left[\frac{\partial}{\partial R^*} \left(\frac{1}{r} \right) \right]_{R^*=R} + \left(\frac{1}{R^* r} \right) \right]_{R^*=R} \right\} d\theta' R d\vartheta dy_1 \quad (23b)$$

After performing the indicated differentiation, equation (23b) can be written as

$$\begin{aligned} \bar{u}_n(\bar{R}, \theta, y) &= \frac{1}{4\pi} \iiint_S \int_{\pi}^{\theta} \frac{-\gamma_c \sin^3 \theta}{\sin^2 \theta'} \left[\frac{\partial}{\partial R^*} \left(\frac{1}{r} \right) \right]_{R^*=R} + \left(\frac{1}{R^* r} \right) \right]_{R^*=R} \sin \theta \\ &\quad - \frac{\bar{R} \gamma_c \sin^3 \sin \theta}{\sin^2 \theta'} \left[\frac{\partial^2}{\partial \bar{R} \partial R^*} \left(\frac{1}{r} \right) \right]_{R^*=R} + \left(\frac{1}{R^*} \right) \left[\frac{\partial}{\partial \bar{R}} \left(\frac{1}{r} \right) \right]_{R^*=R} \right] \} d\theta' R d\vartheta dy_1 \end{aligned} \quad (24)$$

or

$$\begin{aligned} \bar{u}_n(\bar{R}, \theta, y) &= \frac{1}{4\pi} \iint_S -R \gamma_c \sin^3 \sin \theta \int_{\pi}^{\theta} \frac{1}{\sin^2 \theta'} \left[\frac{\partial}{\partial R^*} \left(\frac{1}{r} \right) \right]_{R^*=R} + \left(\frac{1}{R^* r} \right) \right]_{R^*=R} \\ &\quad + \frac{\bar{R} \partial^2}{\partial \bar{R} \partial R^*} \left(\frac{1}{r} \right) \right]_{R^*=R} + \bar{R} \left(\frac{1}{R^*} \frac{\partial}{\partial \bar{R}} \left(\frac{1}{r} \right) \right) \right]_{R^*=R} \} d\theta' d\vartheta dy_1 \end{aligned} \quad (25)$$

The total normal velocity of a point lying on the wing surface ($\bar{R} = R$) must be zero in order for the flow to be tangent to the surface;

hence,

$$\lim_{\bar{R} \rightarrow R} \bar{u}_n(\bar{R}, \theta, y) + V \cos \theta = 0 \quad (26)$$

Since

$$\gamma_c = \frac{\Delta p}{\rho V \sin \theta} \cdot \frac{2V}{2V} = \frac{\Delta C_p V}{2 \sin \theta}, \quad (27)$$

equation (25) can be re-expressed as

$$\begin{aligned} \lim_{\bar{R} \rightarrow R} \frac{\bar{u}_n}{V \sin \theta} &= -\cot \theta \Big|_y = \lim_{\bar{R} \rightarrow R} \frac{1}{4\pi} \iint_S -\frac{R \Delta C_p}{2} \int_{\pi}^{\theta} \left\{ \left(\frac{1}{\sin^2 \theta} \right) \cdot \right. \\ &\cdot \left[\frac{\partial}{\partial R^*} \left(\frac{1}{r} \right) \Big|_{R^*=R} + \left(\frac{1}{R^* r} \right) \Big|_{R^*=R} + \bar{R} \frac{\partial^2}{\partial \bar{R} \partial R^*} \left(\frac{1}{r} \right) \Big|_{R^*=R} + \right. \\ &\left. \left. \bar{R} \left(\frac{1}{R^*} \frac{\partial}{\partial \bar{R}} \left(\frac{1}{r} \right) \right) \Big|_{R^*=R} \right] d\theta' d\vartheta dy_1 \right\} \quad (28) \end{aligned}$$

Now r (see sketch 5) is defined as the straight line distance between a point on the pressure doublet sheet at (R^*, ϑ, y_1) or (x_1, y_1, z_1) and a point on the path of integration (R', θ', y) or (x', y, z) .

$$r = \sqrt{(x_1 - x')^2 + (y_1 - y)^2 + (z_1 - z)^2} \quad (29a)$$

where

$$x_1 = R^* \cos \vartheta \quad (29b)$$

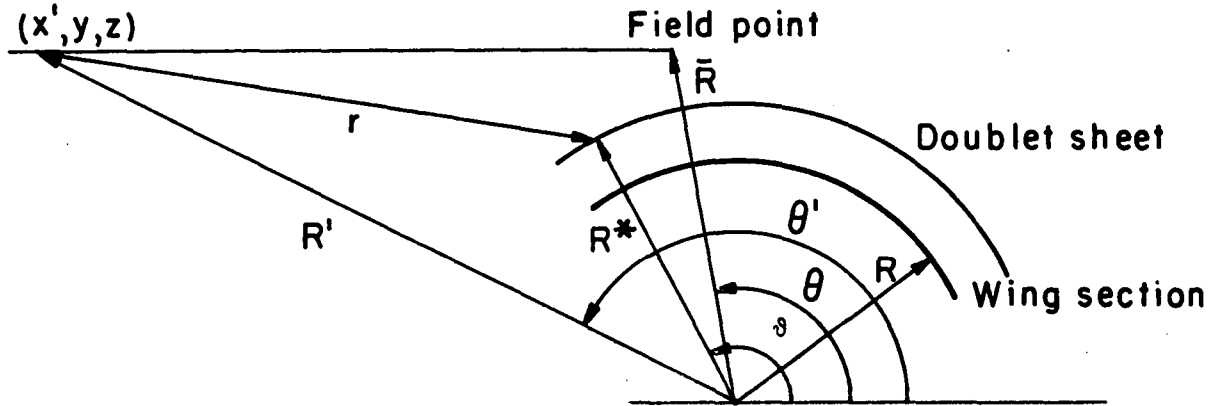
$$x' = R' \cos \theta' = \bar{R} \sin \theta \cot \theta' \quad (29c)$$

$$y_1 = y_1 \quad (29d)$$

$$y = y \quad (29e)$$

$$z_1 = R^* \sin \theta \quad (29f)$$

$$z = R' \sin \theta' = \bar{R} \sin \theta \quad (29g)$$



Sketch 5. Distance between point on pressure doublet sheet and a point on the path of integration

For $R^* = R$, the sheet of pressure doublets is coincident with the wing surface, and for $\bar{R} \rightarrow R$, the field point moves to the surface since this is where the boundary condition of tangent flow must be satisfied. By performing the indicated partial differentiation and then taking the limit as $\bar{R} \rightarrow R$, equation (28) becomes after simplification

$$\begin{aligned}
\cot\theta|_y = & \lim_{\bar{R} \rightarrow R} \frac{R}{8\pi} \iint_S \Delta C_P \left\{ \left[\frac{(y_1 - y)^2}{R} - 2z\sin\vartheta \right] \int_{\pi}^{\theta} \frac{d\theta'}{r^3 \sin^2\theta'} \right. \\
& - 2z\cos\vartheta \int_{\pi}^{\theta} \frac{\cos\theta' d\theta'}{r^3 \sin^3\theta'} + 3z \left(\int_{\pi}^{\theta} \frac{d\theta'}{r^5 \sin^4\theta'} (Rz\sin^2\vartheta) \right. \\
& + \left. \int_{\pi}^{\theta} \frac{\cos\theta' d\theta'}{r^5 \sin^3\theta'} \left[-2Rz\sin\vartheta\cos\vartheta + (y_1 - y)^2 \cos\vartheta \right] \right. \\
& \left. \left. + \int_{\pi}^{\theta} \frac{d\theta'}{r^5 \sin^2\theta'} \left[Rz(\cos^2\vartheta - \sin^2\vartheta) + (y_1 - y)^2 \sin\vartheta \right] \right) \right\} d\vartheta dy_1 \quad (30)
\end{aligned}$$

First Level of Integration

Each of the θ' integrals in equation (30) can be integrated directly by employing the transformation

$$p = \cot\theta' \quad (31)$$

which results in

$$\int_{\pi}^{\theta} \frac{d\theta'}{r^3 \sin^2\theta'} = \frac{1}{z[(R\sin\vartheta - z)^2 + (y_1 - y)^2]} \left[\frac{R\cos\vartheta - z\cot\theta}{\sqrt{D + B\cot\theta + C\cot^2\theta}} - 1 \right] \quad (32a)$$

$$\int_{\pi}^{\theta} \frac{\cos\theta' d\theta'}{r^3 \sin^3\theta'} = \frac{-1}{z^2[(R\sin\vartheta - z)^2 + (y_1 - y)^2]} \cdot$$

$$\cdot \left[\frac{Rz\cos\vartheta\cot\theta - R^2 + 2Rz\sin\vartheta - z^2 - (y_1 - y)^2}{\sqrt{D + B\cot\theta + C\cot^2\theta}} + R\cos\vartheta \right] \quad (32b)$$

$$\int_{\pi}^{\theta} \frac{d\theta'}{r^5 \sin^2 \theta'} = \frac{1}{3z[(R \sin \theta - z)^2 + (y_1 - y)^2]} \left[\frac{R \cos \theta - z \cot \theta}{\sqrt{D + B \cot \theta + C \cot^2 \theta}} \cdot \right. \\ \left. \cdot \left(\frac{1}{D + B \cot \theta + C \cot^2 \theta} + \frac{2}{(R \sin \theta - z)^2 + (y_1 - y)^2} \right) - \frac{2}{(R \sin \theta - z)^2 + (y_1 - y)^2} \right] \quad (32c)$$

$$\int_{\pi}^{\theta} \frac{\cos \theta' d\theta'}{r^5 \sin^3 \theta'} = \frac{1}{3z^2 (D + B \cot \theta + C \cot^2 \theta)^{3/2}} + \frac{R \cos \theta}{z} \int_{\pi}^{\theta} \frac{d\theta'}{r^5 \sin^2 \theta'} \quad (32d)$$

and

$$\int_{\pi}^{\theta} \frac{d\theta'}{r^5 \sin^4 \theta'} = \frac{1}{z^2} \int_{\pi}^{\theta} \frac{d\theta'}{r^3 \sin^2 \theta'} + \frac{1}{z^2} [-R^2 + 2Rz \sin \theta - (y_1 - y)^2] \int_{\pi}^{\theta} \frac{d\theta'}{r^5 \sin^2 \theta'} \\ + \frac{2Rz \cos \theta}{z^2} \int_{\pi}^{\theta} \frac{\cos \theta' d\theta'}{r^5 \sin^3 \theta'} \quad (32e)$$

where

$$r = \sqrt{D + B \cot \theta' + C \cot^2 \theta'} \quad (33a)$$

and

$$D = R^2 - 2Rz \sin \theta + (y_1 - y)^2 + z^2 \quad (33b)$$

$$B = -2Rz \cos \theta \quad (33c)$$

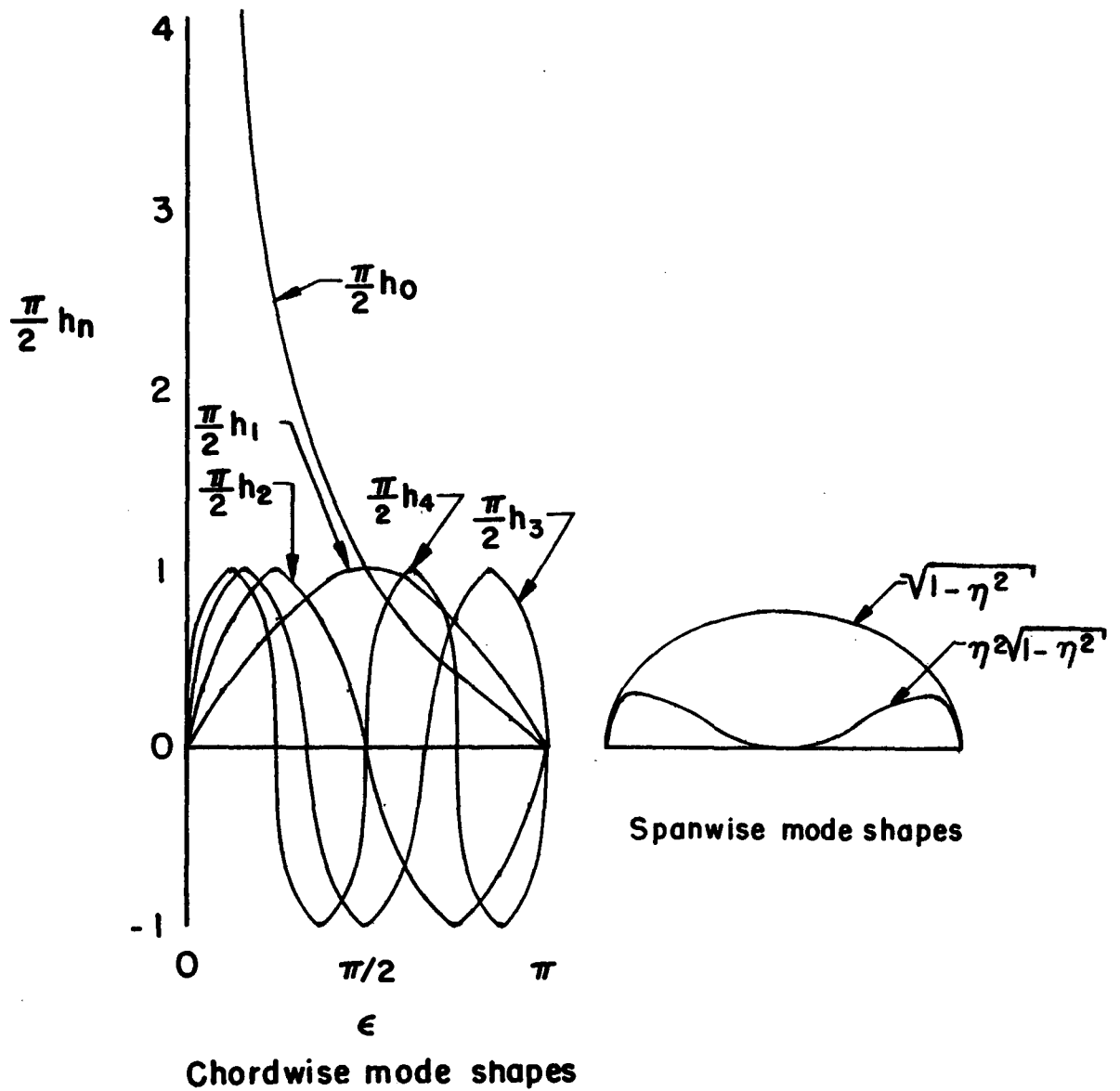
$$C = z^2 \quad (33d)$$

With the substitution of equation (32) into equation (30) and the resultant simplification of terms, the resulting equation is

$$\begin{aligned}
\cot\theta|_y = & \lim_{R \rightarrow R} \frac{R}{8\pi} \iint_S \Delta C_p \left\{ \left[\frac{(y_1 - y)^2}{R} - 2R \sin\theta \sin\vartheta + 3R \sin^2\vartheta \right] \cdot \right. \\
& \cdot \frac{1}{z[(R \sin\vartheta - z)^2 + (y_1 - y)^2]} \left[\frac{R(\cos\vartheta - \cos\theta)}{\sqrt{D + B \cot\theta + C \cot^2\theta}} - 1 \right] \\
& + \frac{2 \cos\vartheta}{z[(R \sin\vartheta - z)^2 + (y_1 - y)^2]} \left[\frac{R^2 \cos\vartheta \cos\theta - R^2 - R^2 \sin^2\theta + 2R^2 \sin\theta \sin\vartheta - (y_1 - y)^2}{\sqrt{D + B \cot\theta + C \cot^2\theta}} \right. \\
& \left. \left. + R \cos\vartheta \right] \right. \\
& + \left[2R^2 (\sin\theta (\cos^2\vartheta - \sin^2\vartheta) + \sin(\sin^2\theta - \cos^2\vartheta)) + (y_1 - y)^2 \right] \cdot \\
& \cdot \left(\sin\vartheta - \sin\theta + \frac{\cos^2\vartheta}{\sin\theta} \right) \left[\frac{1}{[(R \sin\vartheta - z)^2 + (y_1 - y)^2]} \left[\frac{R(\cos\vartheta - \cos\theta)}{\sqrt{D + B \cot\theta + C \cot^2\theta}} \cdot \right. \right. \\
& \cdot \left(\frac{1}{D + B \cot\theta + C \cot^2\theta} + \frac{2}{(R \sin\vartheta - z)^2 + (y_1 - y)^2} \right) - \frac{2}{(R \sin\vartheta - z)^2 + (y_1 - y)^2} \left. \right] \left[\right. \\
& \left. + \left[2R^2 \sin\vartheta \cos(\sin\vartheta - \sin\theta) + (y_1 - y)^2 \cos\vartheta \right] \cdot \right. \\
& \left. \cdot \frac{1}{z(D + B \cot\theta + C \cot^2\theta)^{3/2}} \right\} d\vartheta dy_1 \tag{34}
\end{aligned}$$

Pressure Functions

The unknown ΔC_p distribution appearing in the surface integral of equation (34) is prescribed herein (see sketch 6) to be composed of up to five terms in the Birnbaum series chordwise with the undetermined coefficients being functions of spanwise position.



Sketch 6. Loading mode shapes.

Hence,

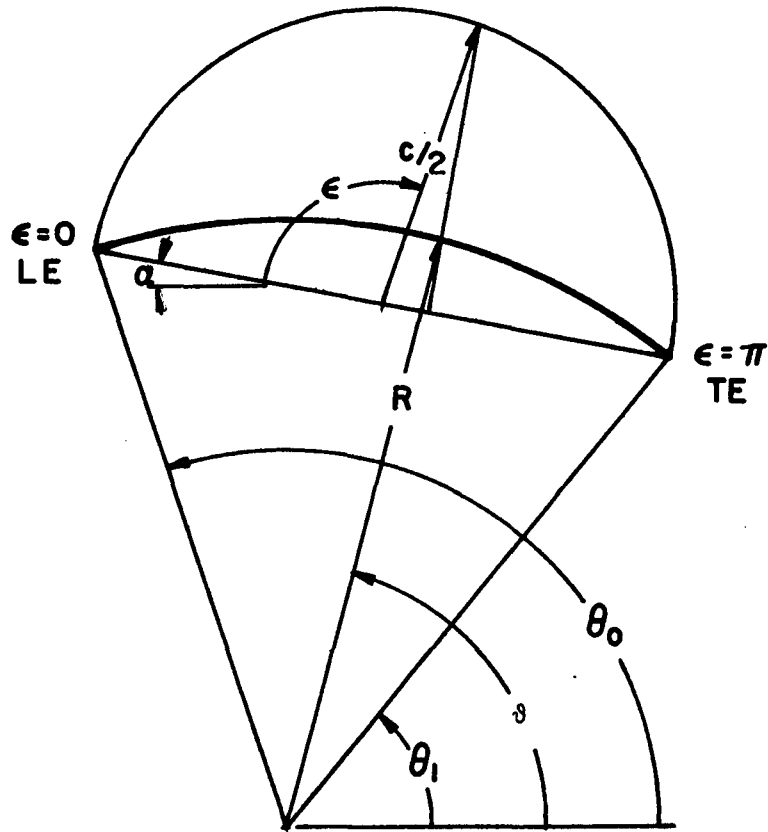
$$\Delta C_p(\epsilon, y_1) = \sum_{n=0}^{N-1} \sum_{\substack{m=0 \\ \text{even}}}^2 c_{nm} \left(\frac{y_1}{b/2} \right)^m \sqrt{1 - \left(\frac{y_1}{b/2} \right)^2} h_n(\epsilon) \quad (35a)$$

where

$$h_0(\epsilon) = \frac{2}{\pi} \cot \frac{\epsilon}{2}, \quad n = 0 \quad (35b)$$

and

$$h_n(\epsilon) = \frac{2}{\pi} \sin n\epsilon, \quad 1 \leq n \leq 5 \quad (35c)$$



Sketch 7. Relationship between ϵ and θ .

Final Form of Integral Equation

Since the chordwise pressure modes are defined in terms of a variable, ϵ , which goes from zero at the leading edge to π at the trailing edge, it is necessary to change the chordwise variable used in the surface integration from ϑ to ϵ . Sketch 7 shows the equivalent edge locations in the ϵ and ϑ coordinate variables.

The general expression relating ϵ and ϑ is

$$\epsilon = \cos^{-1} \left\{ 1 - \frac{2R}{c} \left[\cos(\vartheta + \alpha) - \cos(\vartheta_o + \alpha) \right] \right\} \quad (36a)$$

and so

$$d\vartheta = -\frac{c}{2R} \frac{\sin \epsilon \, d\epsilon}{\sin(\vartheta + \alpha)} \quad (36b)$$

Hence, by combining equations (34), (35a), and (36b), the following equation results:

$$\cot\theta|_y = \lim_{R \rightarrow R} \frac{-R}{8\pi} \sum_{n=0}^{N-1} \sum_{\substack{m=0 \\ \text{even}}}^2 c_{nm} \int_{-b/2}^{b/2} \frac{c\eta^m \sqrt{1-\eta^2}}{2R} \int_{\pi}^0 h_n(\epsilon) \left\{ \frac{\sin \epsilon \, d\epsilon \, dy_1}{\sin(\vartheta + \alpha)} \right\}^{\dagger} \quad (37a)$$

which can be written in a more convenient form as simply

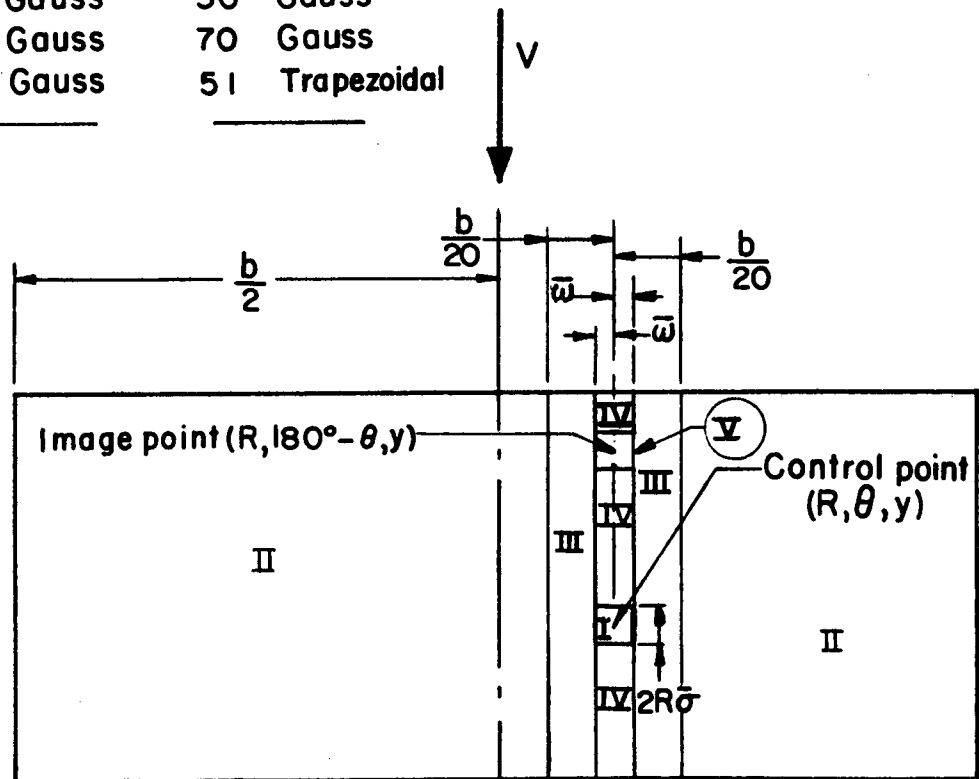
$$\cot\theta|_y = \lim_{R \rightarrow R} \frac{c}{16\pi} \sum_{n=0}^{N-1} \sum_{\substack{m=0 \\ \text{even}}}^2 c_{nm} \int_{-b/2}^{b/2} \eta^m \sqrt{1-\eta^2} \int_0^{\pi} h_n(\epsilon) \left\{ \frac{\sin \epsilon \, d\epsilon \, dy_1}{\sin(\vartheta + \alpha)} \right\}^{\dagger} \quad (37b)$$

[†]See equation (34) for this expression.

General Surface Integrations

Since the θ' integrals have been determined and the pressure mode shapes specified, the surface integration can now be considered. This is accomplished, in general, by means of numerical quadrature. The quadrature basically employed is Gaussian in both directions with the exceptions (as shown in Sketch 8) over the spanwise range which

Number of Integration Steps				
Region	Chordwise		Spanwise	
I				
II	50	Gauss	30	Gauss
III	100	Gauss	70	Gauss
IV	200	Gauss	51	Trapezoidal
V				



Sketch 8. Integration regions and number of integration points used in each for low-to-moderate camber.

correspond to the width of the square boxes centered around the control and its image point, the image point only occurring when

$$\theta_0 \leq 180^\circ - \theta \leq \theta_1 .$$

In this spanwise range, 51 evenly spaced points are employed in the trapezoidal rule integration, and Gaussian quadrature, which employs 200 steps divided according to arc length ahead of and behind the boxes, is used chordwise. The number of Gaussian steps and trapezoidal rule points have been established by convergence studies for an aspect ratio 20 rectangular wing with a box length of .01 chord and a camber ratio of .00125 at $\alpha = 5^\circ$. This set of integration steps and box length have also been found to be adequate for cambered wings of other aspect ratio.

Because numerical integration cannot be carried out across the high-ordered singularity which exists at the control point, of the form

$$\frac{1}{\Delta z^2 + \Delta y^2} - \frac{1}{r^3} ,$$

this area is split off from the general surface

integration and is treated separately. The image point, which is the cambered wing equivalent of the flat wing singular strip, has a

singularity of the form $\frac{1}{\Delta z^2 + \Delta y^2}$ and $\left[\frac{1}{\Delta z^2 + \Delta y^2} \right]^2$; hence, the

box surrounding it must also be broken off and treated separately. The procedures employed are described in the following sections.

Surface Integration Over the Control-Point Box

The surface integration over the box is accomplished by:

- (1. establishing basic expansion variables for small spanwise and

angular displacements away from the control point; (2. using these expansions to approximate each fundamental form which appears inside the braces in equation (34); and (3. using finite part concepts, integrate the resulting combination of forms over the box.

Expansions

The expansion variables in which the expansion process is to be conducted are

$$y_1 = y + \omega \quad (38)$$

and

$$\vartheta = \theta + \sigma \quad (39)$$

where ω and σ are the small positive displacements in the spanwise and angular directions, respectively. The angular displacement is chosen in terms of ϑ rather than ϵ (the coordinate in which the loading is specified) in order to simplify the expansion process.

Approximate Forms

By employing the above expansion variables, the following approximate forms are obtained near the control point for the general expressions given in equation (34). They are to $O(\omega^2)$ and $O(\sigma^2)$:

$$\begin{aligned} \frac{(y_1 - y)^2}{R} - 2R \sin \theta \sin \vartheta + 3R \sin^2 \vartheta \doteq \frac{\omega^2}{R} + R(\sin^2 \theta - 2\sigma^2 \sin^2 \theta + \\ 3\sigma^2 \cos^2 \theta + 4\sigma \sin \theta \cos \theta) \end{aligned} \quad (40a)$$

$$(R\sin\vartheta - z)^2 + (y_1 - y)^2 \doteq R^2\sigma^2\cos^2\theta + \omega^2 \quad (40b)$$

$$D + B \cot\theta + C \cot^2\theta \doteq R^2\sigma^2 + \omega^2 \quad (40c)$$

$$R(\cos\vartheta - \cos\theta) \doteq -R \frac{\sigma^2}{2} \cos\theta + \sigma\sin\theta \quad (40d)$$

$$\cos\vartheta \doteq \left(1 - \frac{\sigma^2}{2}\right) \cos\theta - \sigma\sin\theta \quad (40e)$$

$$\begin{aligned} R^2\cos\vartheta \cos\theta - R^2 - R^2\sin^2\theta + 2R^2\sin\theta\sin\vartheta - (y_1 - y)^2 \doteq \\ - [R(\sigma^2/2)(1+\sin^2\theta) + \omega^2 - R^2\sigma\sin\theta\cos\theta] \end{aligned} \quad (40f)$$

$$\begin{aligned} 2R^2[\sin\theta(\cos^2\vartheta - \sin^2\vartheta) + \sin\vartheta(\cos^2\theta - \cos^2\vartheta)] \doteq \\ (-\sigma\cos\theta + \frac{3}{2}\sigma^2\sin\theta - \sigma^2\sin^3\theta) 2R^2 \end{aligned} \quad (40g)$$

$$(y_1 - y)^2 \sin\vartheta - \sin\theta + \frac{\cos^2\vartheta}{\sin\theta} \doteq \omega^2 \frac{\cos^2\theta}{\sin\theta} \quad (40h)$$

$$\begin{aligned} 2R^2\sin\vartheta \cos\vartheta (\sin\vartheta - \sin\theta) + (y_1 - y)^2\cos\vartheta \doteq 2R^2[\sigma\sin\theta\cos^2\theta \\ + \sigma^2(\cos\theta - \frac{5}{2}\sin^2\theta\cos\theta)] + \omega^2\cos\theta \end{aligned} \quad (40i)$$

These approximate forms are generally applicable for all angular locations of control points between θ_0 and θ_1 . An exception to this is at $\theta = 90^\circ$ where the approximate form of $(R\sin\vartheta - z)^2 + (y_1 - y)^2$, that is, $R^2\sigma^2\cos^2\theta + \omega^2$, tends to simply ω^2 . If more terms are retained in the

original expansion of the above expression a more accurate result is obtained and it is

$$R^2 \left[\frac{\sigma^4}{4} \sin^2 \theta + \sigma^2 \cos^2 \theta - \sigma^3 \sin \theta \cos \theta \right] + \omega^2$$

It can be shown that this more general form tends toward the original form for $\left(\frac{\sigma}{2} - \cot \theta\right)^2 \ll 2 \cot^2 \theta$ and tends to $R^2 \frac{\sigma^4}{4} + \omega^2$ for $\theta \rightarrow 90^\circ$, a much different result than obtained previously.

Both approximate forms, when used, would appear in the denominator and hence be singular in σ . However, the more general form would be singular in σ to an order higher than that encountered with the original form (σ^4 vs. σ^2) and hence lead to new expressions to be integrated. These integrations show that the box contribution to be just the $\theta = 90^\circ$ limit of the θ not near 90° solution (original approximate form) whose development follows.

From a practical standpoint $\theta = 90^\circ$ should be avoided as a control point location so that numerical difficulties outside the box associated with the higher ordered singularities can be circumvented. It has been found that in order to assure convergence of the numerical integrations $|\theta - 90^\circ|$ should be less than 1.5° .

Integrated Results

With these approximated forms substituted into equation (34), the surface integration over the box becomes

$$\begin{aligned}
& \lim_{R \rightarrow R} \frac{R}{8\pi} \int_{-\bar{\omega}}^{\bar{\omega}} \int_{-\bar{\sigma}}^{\bar{\sigma}} \Delta C_p(\theta, y) \left\{ \left[\frac{\omega^2}{R} + R(\sin^2\theta - 2\sigma^2 \sin^2\theta + 3\sigma^2 \cos^2\theta \right. \right. \\
& \quad \left. \left. + 4\sigma \sin\theta \cos\theta \right] \frac{-1}{z(R^2 \sigma^2 \cos^2\theta + \omega^2)} \left[\frac{R[(\sigma^2/2)\cos\theta + \sigma \sin\theta]}{\sqrt{R^2 \sigma^2 + \omega^2}} + 1 \right] \right. \\
& \quad \left. + \frac{-(2 - \sigma^2)\cos\theta + 2\sigma \sin\theta}{z(R^2 \sigma^2 \cos^2\theta + \omega^2)} \left[\frac{R^2(\sigma^2/2)(1 + \sin^2\theta) - R^2 \sigma \sin\theta \cos\theta + \omega^2}{\sqrt{R^2 \sigma^2 + \omega^2}} \right. \right. \\
& \quad \left. \left. + R((1 - \sigma^2/2)\cos\theta - \sigma \sin\theta) \right] \right. \\
& \quad \left. + [(-\sigma \cos\theta + \frac{3}{2} \sigma^2 \sin\theta - \sigma^2 \sin^3\theta)2R^2 + \omega^2 \cos^2\theta / \sin\theta] \right. \\
& \quad \cdot \left[\frac{1}{R^2 \sigma^2 \cos^2\theta + \omega^2} \left[\frac{R[(\sigma^2/2)\cos\theta + \sigma \sin\theta]}{\sqrt{R^2 \sigma^2 + \omega^2}} \left(\frac{1}{R^2 \sigma^2 + \omega^2} + \frac{2}{R^2 \sigma^2 \cos^2\theta + \omega^2} \right) \right. \right. \\
& \quad \left. \left. - \frac{2}{R^2 \sigma^2 \cos^2\theta + \omega^2} \right] \right] + \left[2R^2 \left(\sigma \sin\theta \cos^2\theta + \sigma^2(\cos\theta - 5/2 \sin^2\theta \cos\theta) \right) \right. \\
& \quad \left. \left. + \omega^2 \cos\theta \right] \frac{1}{z(R\sigma^2 + \omega^2)^{3/2}} \right\} d\sigma d\omega \tag{41}
\end{aligned}$$

where

$$R\bar{\sigma} = \bar{\omega} \tag{42}$$

This integral expression can be integrated[†] with any standard set of integral tables, such as reference 22, and the result is to $\mathcal{O}(\bar{\sigma}^0)$ (to be read order of $\bar{\sigma}$ to the zeroth power, i.e., σ independent terms)

[†]See appendix A for an example of the manner in which the integrations must be conducted.

$$4\sin\theta \left[1 - \frac{\cos^2\theta}{3} + \frac{\cos^4\theta}{5} \cdot \cdot \cdot \right] \Delta C_p(\theta, y) \quad (43)$$

where

$$\Delta C_p(\theta, y) = \sum_{n=0}^{N-1} \sum_{\substack{m=0 \\ \text{even}}}^2 \left(\frac{y}{b/2} \right)^m \sqrt{1 - \left(\frac{y}{b/2} \right)^2} h_n(\epsilon_\theta) \quad (44)$$

There are some interesting features of this box integration result. The first is that the lowest ordered non-zero result does not depend on the box size. The second is that, like the flat-wing solution (unpublished analysis performed by Mr. P. J. Bobbitt), the leading term is determined to be basically a $4\Delta C_p(\theta, y)$. Thirdly, the cosine terms can be thought of as an $\mathcal{O}(\bar{\sigma})$ camber correction to the flat-wing solution ($\theta \doteq 90^\circ$), which becomes more important as the camber increases. Fourthly, the $\mathcal{O}(\bar{\sigma})$ terms which are omitted can also become important for θ angles near 0° and 180° because there the $\mathcal{O}(\bar{\sigma}^0)$ terms approach zero. However, since the effect of the $\mathcal{O}(\bar{\sigma}^0)$ terms can be controlled by selecting small values of $\bar{\sigma}$, and since some of the $\mathcal{O}(\bar{\sigma})$ terms were obtained by expanding about $\theta = 90^\circ$, the results presented herein are only accurate to $\mathcal{O}(\bar{\sigma}^0)$. Hence, solutions for very large camber ratios, which lead to θ angles near 0° and 180° , are attempted with caution - as should those employing the slope-projection technique.

Surface Integration Over the Image-Point Box

The same procedures used in arriving at the expanded form of the

general expression are employed about the image point, with the exception that, instead of expanding about θ , the angular expansions take place about $180^\circ - \theta$. This only changes the signs on the $\cos\theta$ terms which result from the terms $\sin(180^\circ - \theta + \sigma)$ and $\cos(180^\circ - \theta + \sigma)$. When these changes are followed through the simplified integral equation, integrands which yield the $\mathbf{O}(\bar{\sigma}^0)$ terms are determined to be identical to those for the control point box, but they do have slightly different coefficients. Thus, the image point contribution to the normal induced velocity at the control point is to $\mathbf{O}(\bar{\sigma}^0)$

$$\left(1 + \frac{\cos\theta}{|\cos\theta|}\right) 4\sin\theta \left[1 - \frac{\cos^2\theta}{3} + \frac{\cos^4\theta}{5} \dots\right] \Delta C_p(180^\circ - \theta, y) \quad (45)$$

This is an interesting result in that for control points in the first quadrant (image point ahead of control point) the term $\left(1 + \frac{\cos\theta}{|\cos\theta|}\right)$ becomes 2, and for control points in the second quadrant (image point behind control point) the term $\left(1 + \frac{\cos\theta}{|\cos\theta|}\right)$ is zero. The behavior of this term is identical to that of the modified kernel function in the flat-wing solution at the spanwise location of the singularity.

Solution Technique

The solution of the subsonic integral equation given in equation (34) is made by requiring that the flow be tangent to the surface at a number of control points. There are as many control points as there are pressure mode-shape combinations. For each control point, the surface integrals are evaluated either numerically or analytically for each mode-shape combination. The sum of these

integrations is stored along a row of matrix A. The unknown coefficients of the pressure mode-shape combinations, c_{nm} , are determined after both the boundary condition value and influence coefficient matrices are filled by solving the matrix equation

$$\{\cot\theta|_y\} = [A] \{c_{nm}\} \quad (46)$$

VIII. RESULTS AND DISCUSSION

General

In this chapter the results of calculations made using the present method with various box sizes, control point locations and number of control points are analyzed followed by a discussion of results for specific wings. The first wing results presented are for a flat rectangular planform for which experimental data are available and are of interest primarily for the check it provides of the present method. Cambered wing comparisons are only made on a theoretical basis because an extensive literature search uncovered only one paper (ref. 22) containing experimental data for cambered wings of the type considered herein. Unfortunately most of these data were obtained with the wing having some regions of separated flow. This happened because the airfoil shapes used were developed from thin plates which had only simple rounding at the leading edge and hence did not promote flow attachment. The present method is developed for attached flow conditions and hence not applicable to these data.

The theoretical results used to compare with those of the present method come from methods which account for camber by the slope-projection technique with the lifting surface constrained to the X-Y plane; in particular, the methods of Scholz (ref. 23) and Multhopp (ref. 8). Comparisons are made for rectangular wings over an aspect ratio, camber ratio and α range.

Applications to rectangular wings of aspect ratio less than four are not attempted with the present method because only two spanwise

loading modes are employed. These two modes provide for only two spanwise rows of control points on a panel and are insufficient to insure tangent flow when the induced effects are large across the span. The use of additional spanwise modes from the same series (eq. (35a)) would allow for more spanwise rows of control points and hence provide better solutions. However, this is not attempted herein because of the substantial increase required in computer time.

A study is also conducted using two-dimensional theory for a highly cambered section to: (1) provide limiting values for the three-dimensional results, and (2) establish relationships between the results at two different angles of attack which can be compared with those of the three-dimensional analysis.

Variation of Results With-

Box Size

The integrations over the box of the approximated singular and nonsingular terms have yielded a result which is independent of the box size to $O(\bar{\sigma}^0)$. However, the size of the box can still have an effect on the answers by being either too large or too small. If the box is too large, it will include those portions of the wing which are outside the valid range of the functions approximating the singular part of the integrands. If, however, the box is too small the numerical integrations outside the box will suffer a loss in accuracy, unless substantially more integration stations are used, because of the close proximity of the edge of the box to the singularities. These two extremes are illustrated in Table I.

TABLE I.

Number of Integration Stations Required for Different Box Sizes
and Effect of Box Size on Aerodynamic Characteristics for an
 $A = 20$, $h/c = .00125$ Rectangular Wing at $\alpha = 5^\circ$.
Control Points at $x/c = .345, .905$.

Box Size	Integration Steps in Box Strip		Aerodynamic Characteristics			
	Chordwise	Spanwise	C_L	x_{cp}	$C_{D,i}$	$C_{D,ii}$
.1	200	51	.5332	.2524	.0048	-.0008
.01	200	51	.4959	.2559	.0042	.0034
.001	300	151	.5121	.2544	.0044	.0017
.0001	500	201	.4450	.3212	.0034	.0212

Spanwise Control Point Locations

Only two spanwise rows of control points are utilized along a semispan because only two spanwise loading modes are employed in the present analysis. A limited study of the effects on the aerodynamic characteristics of varying the location of these rows was made and the results, presented in Table II, show only slight variation with row location set. However, the 0.25, 0.75 set was chosen to be used

TABLE II.

Effect of Spanwise Location of Control Point Rows
on Aerodynamic Characteristics of an
 $A = 20$, $h/c = .00125$ Rectangular
Wing at $\alpha = 5^\circ$. Control
Points at $x/c = .345, .905$

$2y/b$	C_L	x_{cp}	$C_{D,i}$	$C_{D,ii}$
0, .7070	.4950	.2562	.0041	.0031
.25, .75	.4961	.2561	.0042	.0035
0, .8165	.5125	.2557	.0045	.0024

subsequently because it (1) resulted in the closest agreement between the two induced drag values and (2) because of symmetry represents a solution which constrains the flow at two additional control points on the left half of the wing as opposed to the total of three which result for a set with zero as one of the spanwise locations.

The induced drag terms $C_{D,i}$ and $C_{D,ii}$ are called the far-field and near-field results, respectively. $C_{D,i}$ is determined by the method of reference 6, and $C_{D,ii}$ from the combination of the distributed camber drag and the leading-edge suction as seen in appendix B. Exact numerical agreement between these two drag terms is taken to mean that the chord loading is correct and hence the best solution has been reached. In practice, exact agreement is seldom achieved, hence chordwise control point patterns which yield reasonably close agreement between the two drag terms are chosen subsequently (as above for the spanwise sets) as the ones to be used.

Chordwise Control Point Locations

For two control points, many placement patterns were investigated, as shown in Table III. From the table, it is evident that, for the first control point near $x/c = 0.35$, the variations of the aerodynamic characteristics for the $A = 5$, $h/c = 0.00125$ rectangular wing at $\alpha = 5^\circ$ are reduced, especially those of the induced drag coefficient. By comparing the two induced drag terms in the table the closest agreement is seen to occur when the second control point is at $x/c = 0.80$ or 0.95 . These locations are so near those prescribed by Multhopp in reference 6 for a two chordal loading solution, that is, $x/c = 0.345$ and 0.905 that these are used in the present method for

the two chordal loading solution. For higher camber ratios additional chordwise control points and loading functions are needed to effect a best solution as seen in the next section.

TABLE III

Effect of Locating Two Control Points on the Aerodynamic Characteristics of an $A = 5$, $h/c = .00125$ Rectangular Wing at $\alpha = 5^\circ$

Control Point Locations		Aerodynamic Characteristics			
First	Second	C_L	x_{cp}	$C_{D,i}$	$C_{D,ii}$
.1	.9	.3839	.2398	.0095	.0060
.15	.80	.3766	.2433	.0092	.0070
.20	.80	.3764	.2446	.0092	.0071
.20	.90	.3803	.2462	.0094	.0073
.25	.75	.3739	.2440	.0090	.0071
.25	.95	.3823	.2479	.0095	.0075
.35	.65	.3724	.2463	.0090	.0076
.35	.75	.3740	.2474	.0090	.0076
.35	.80	.3759	.2485	.0091	.0078
.35	.85	.3774	.2495	.0092	.0078
.35	.90	.3784	.2500	.0093	.0079
.35	.95	.3801	.2511	.0094	.0081

Number of Chordal Control Points

The number of control points must increase with camber in order that the flow might be constrained to approximate better the normal velocity distribution or camber shape. If only two chordwise control points, hence loading functions are used, the aerodynamic characteristics which result would lose accuracy, especially those involving the pitching moment, because it depends more heavily on the third and higher modes than do the lift and leading-edge suction.

The effect of number and locations of control points on the aerodynamic characteristics is tabulated in Table IV for a typical wing. From this table it can be seen that there are several patterns which would appear to do equally as well from a best solution check.

TABLE IV

Effect of Number and Locations of Control Points on the Aerodynamic Characteristics of an $A = 5$, $h/c = 0.0314$ Rectangular Wing at $\alpha = 5^\circ$

Control Point Locations					Aerodynamic Characteristics			
First	Second	Third	Fourth	Fifth	C_L	x_{cp}	$C_{D,i}$	$C_{D,ii}$
.345	.905				.8798	.3761	.0498	.0077
.05	.35	.95			.9936	.3865	.0633	.0580
.1	.32	.8			-.0028	13.6321	.0000	-.2656
.1	.32	.9			.5202	.5531	.0176	-5.6964
.17	.4	.95			.5939	.0773	.0229	-2.0950
.19	.615	.95			.3877	1.3917	.0101	-.9160
.45	.7	.95			.7685	.4995	.0382	.0504
.52	.78	.98			.8482	.4038	.0464	.0361
.05	.35	.65	.95		.8363	.4215	.0451	.0561
.05	.35	.75	.95		.8334	.4223	.0448	.0561
.1	.2	.8	.9		.5776	.5334	.0218	.0398
.1	.32	.6	.97		-.3227	.8174	.0510	-1.5160
.116	.414	.75	.97		-3.1421	-.3092	.6342	-68.5122
.2	.4	.6	.8		.1356	-2.5608	.0016	-2.2424
.05	.32	.55	.75	.95	.8517	.4296	.0468	.0583
.08	.29	.57	.83	.98	.8098	.4756	.0424	.0653
.1	.32	.5	.7	.9	-3.8451	.0277	1.0037	-71.4019

In order to try and determine if there was a preferential set of chordwise control points, a separate computer program was developed which solved equation (46) for the left-hand side using the previously determined $\{c_{nm}\}$. Hence, the variations from the tangency flow condition for points in between the control points could be examined and some indication of the best control point patterns obtained. From this study the pattern of $x/c = 0.05, 0.35, 0.65, 0.95$ was determined to be the best choice. It should be noted that this set may not be usable throughout the angle-of-attack range, for if one of these control points falls within the range $88.5^\circ < \theta < 91.5^\circ$ a new point must be selected to avoid the numerical integration problems discussed in Chapter VII. In addition, this pattern may not be appropriate for wings of other camber or aspect ratio.

Experimental Data Comparison

Since the only reliable data available with which to compare was for flat rectangular wings, the present method, which is only valid for cambered wings, was studied numerically to determine what value of h/c would adequately represent a flat wing. A value of $h/c = 0.000013$ was determined to be sufficiently small, as further small reductions in h/c didn't change the numerical results. Two chordal loading modes with the associated control points already established were employed in obtaining solutions. The results of the computations, along with those of the modified Multhopp method (ref. 8), are presented in Table V and compared with those from the experiment on both a section and wing basis.

Further, all three lifting pressure distributions are given in figure 1 at the plane of symmetry for an $A = 4$ rectangular wing at $\alpha = 4.35^\circ$.

TABLE V

Experimental and Theoretical Aerodynamic
Characteristics for an $A = 4$ Flat
Rectangular Wing

Type	$2y/b = 0 : \alpha = 4.35^\circ$		C_{L_α}	x_{cp}
	c_l	x_{cp}		
Experiment (ref. 24)	.323	.244	.060	.235
Present Method (N=2) (2 semispan stations)	.346	.242	.067	.237
Modified Multhopp Method (N=4) (19 semispan stations)	.331	.240	.063	.230

Both the table and the figure show that the present method produces results which agree reasonably well with the experiment and the modified Multhopp method. Thus, having shown that the present method yields reliable results for flat wings, it is of interest to determine its efficacy for cambered wings. Because of the lack of reliable cambered wing data obtained for rectangular planforms meeting the camber constraint of the present method, as mentioned in the Introduction, cambered wing correlations are made with results obtained with the exact two-dimensional method given in appendix C.

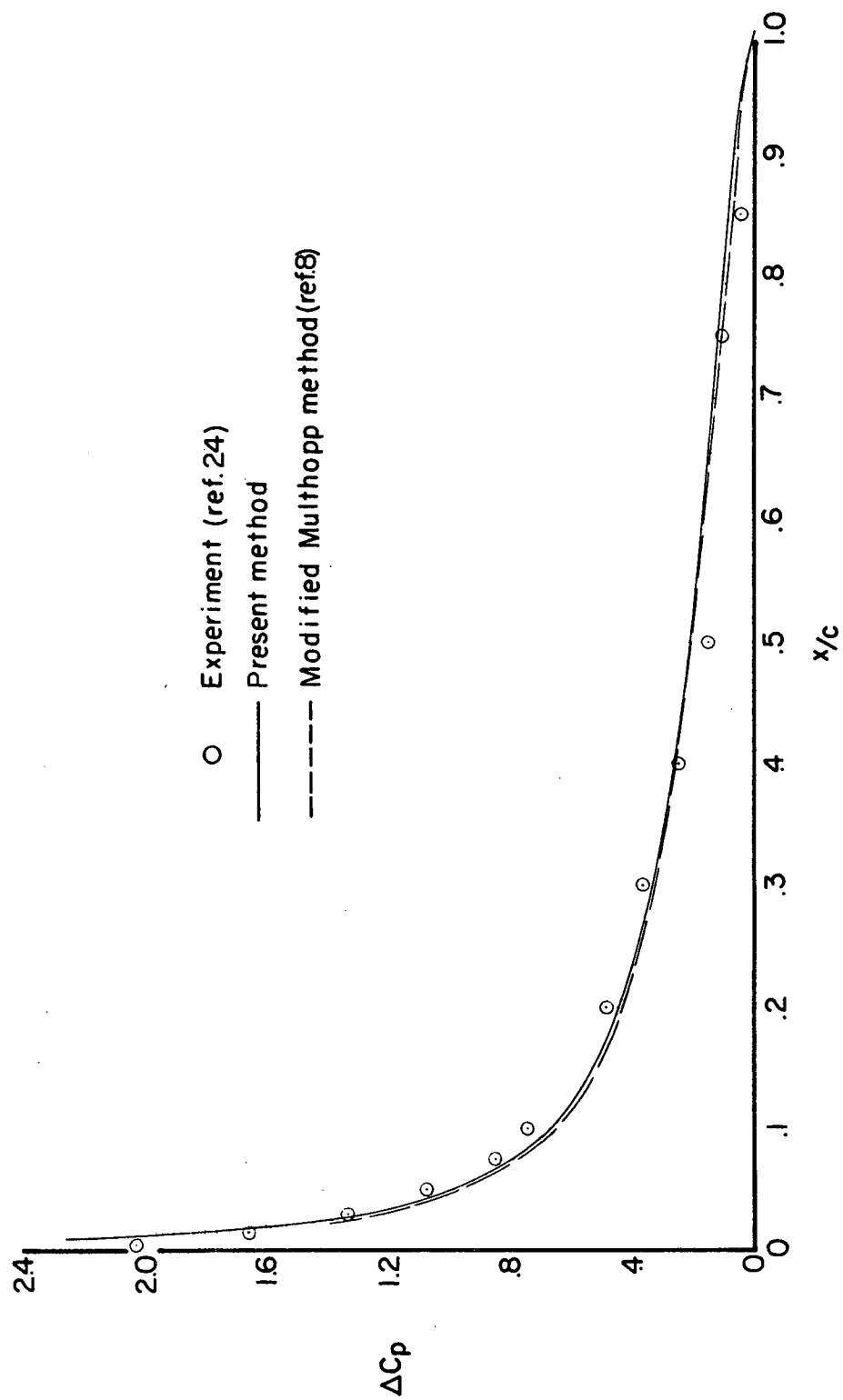


Figure 1.- Lifting pressure coefficient distribution for $A = 4$ flat rectangular wing at $2y/b = 0$ and $\alpha = 4.35^\circ$.

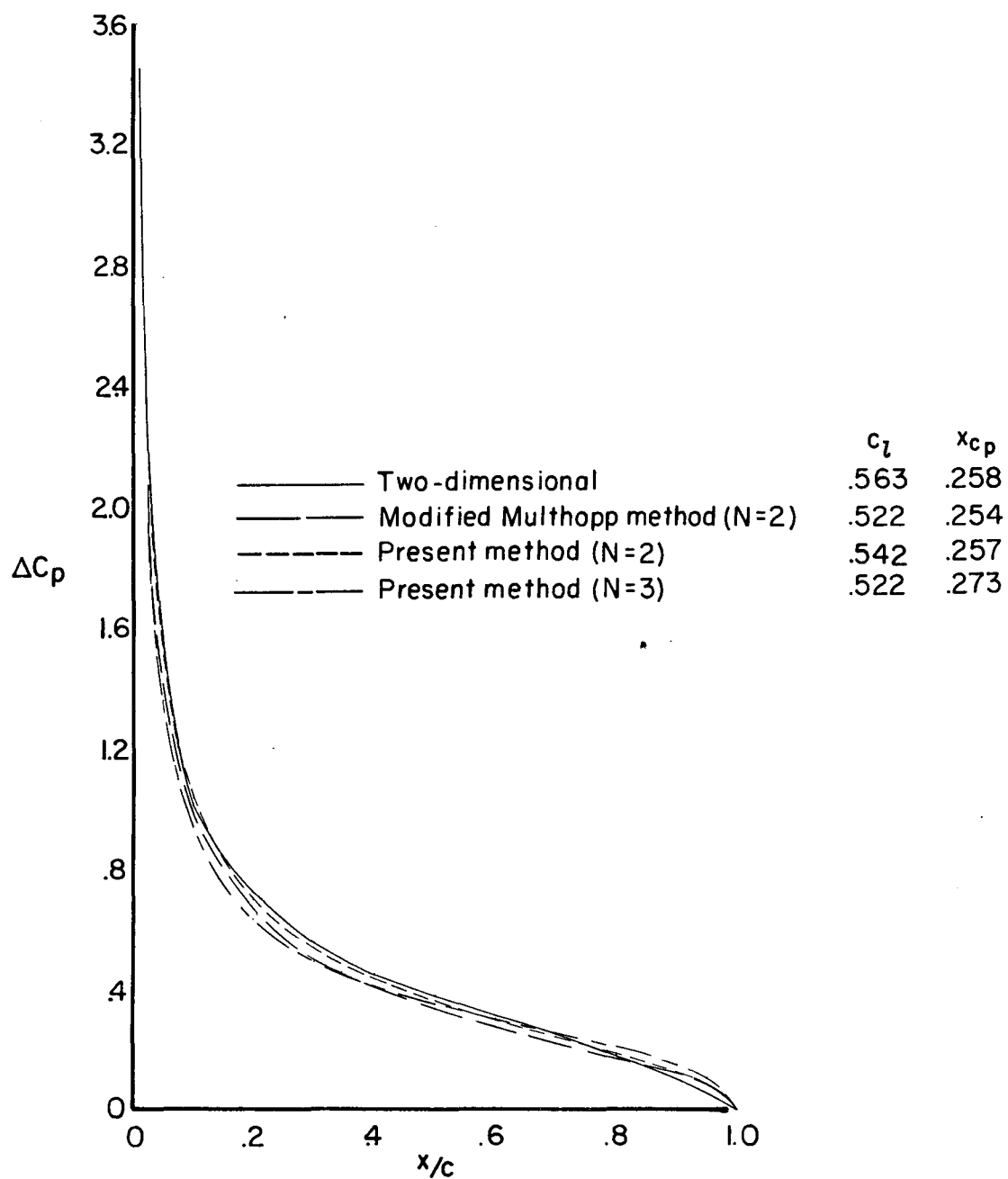
Theoretical Comparisons

Two- and Three-Dimensional Lifting Pressures

The lifting pressures for the two-dimensional transformed solution (appendix C) are compared with those of the present method and modified Multhopp method at the plane of symmetry of an aspect ratio 20 rectangular wing, with all having $h/c = 0.00125$ and at $\alpha = 5^\circ$. The results are graphed in figure 2(a) and show that the present method for $N = 2$ agrees better with the two-dimensional than $N = 3$ for the present method or $N = 2$ for the modified Multhopp method. A similar graph is presented in figure 2(b) for $h/c = 0.0314$ and $\alpha = 5^\circ$ with $N = 4$ for the present method and $N = 4$ for the modified Multhopp method. A comparison of the three sets of data shows that the present method predicts better the two-dimensional c_l value, whereas the modified Multhopp predicts better the x_{cp} value and lifting pressure distribution. The poor quality of the lifting pressure distribution predicted by the present method is serious and is discussed later.

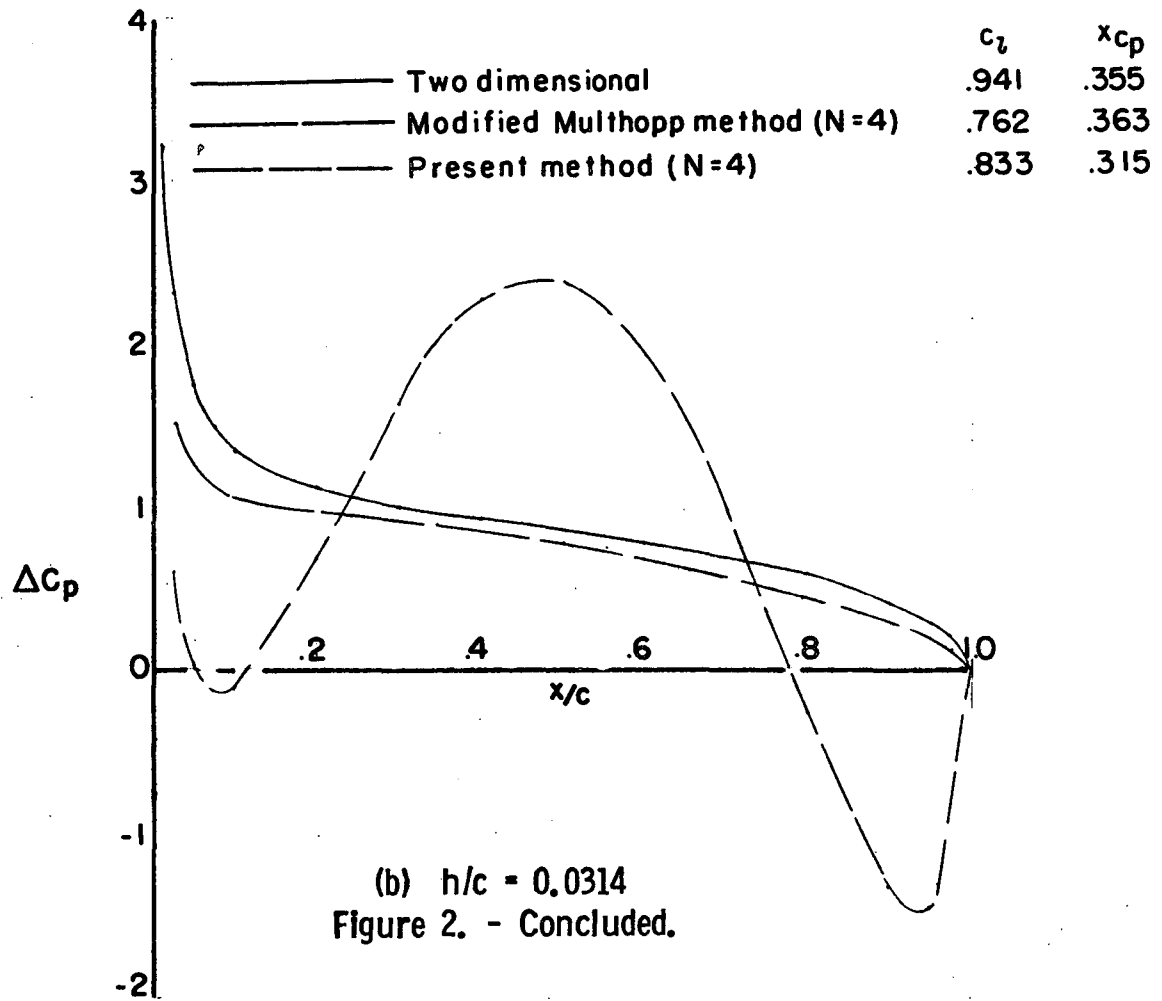
Two-Dimensional Cambered Wings

The prediction of the aerodynamic characteristics for two-dimensional circular-arc-cambered wings can be accomplished in either of two ways. The first is in the classic manner of transforming a circle into the airfoil shape and arriving at the moment and forces by Blasius' theorems as given in appendix C (referred to herein as the



(a) $h/c = 0.00125$

Figure 2.- Lifting pressure coefficient distribution for three-dimensional methods at $A = 20$ and $2y/b = 0$ and two-dimensional exact method, all at $\alpha = 5^\circ$.



(b) $h/c = 0.0314$
Figure 2. - Concluded.

transform method.) The second is based on thin airfoil theory (small α and h/c approximations) and employs the Birnbaum series to represent the chord loading and from which the moment and forces are determined (Reference 25 has examples of the procedures.). When the results of these two methods are compared in Table VI for $h/c = 0.50$ and α values of 0° and 5° , remarkable agreement is noted for both the x_{cp} and c_l values. In order to understand this agreement, the chord loading predicted by each method at $\alpha = 5^\circ$ is graphed and appears in figure 3. An examination of this figure shows noticeable disagreement in lifting pressures along the chord; however, the integrated effect of these differences is seen from Table VI to be small because of the compensating behavior of the disagreements.

TABLE VI

Circular-Arc Lift and Center of Pressure

Method	c_l Equation	x_{cp} Equation
Transform	$2\pi[\sin\alpha + 2(h/c)\cos\alpha]$	$-\frac{\frac{\sin\alpha \cos\alpha}{2} - \sin\alpha - \cos\alpha\left(\frac{2h}{c}\right)}{c_l/\pi}$
Thin airfoil	$2\pi\left(\frac{\alpha\pi}{180} + 2\frac{h}{c}\right)$	$\frac{1}{4} + \frac{\pi(h/c)}{c_l}$

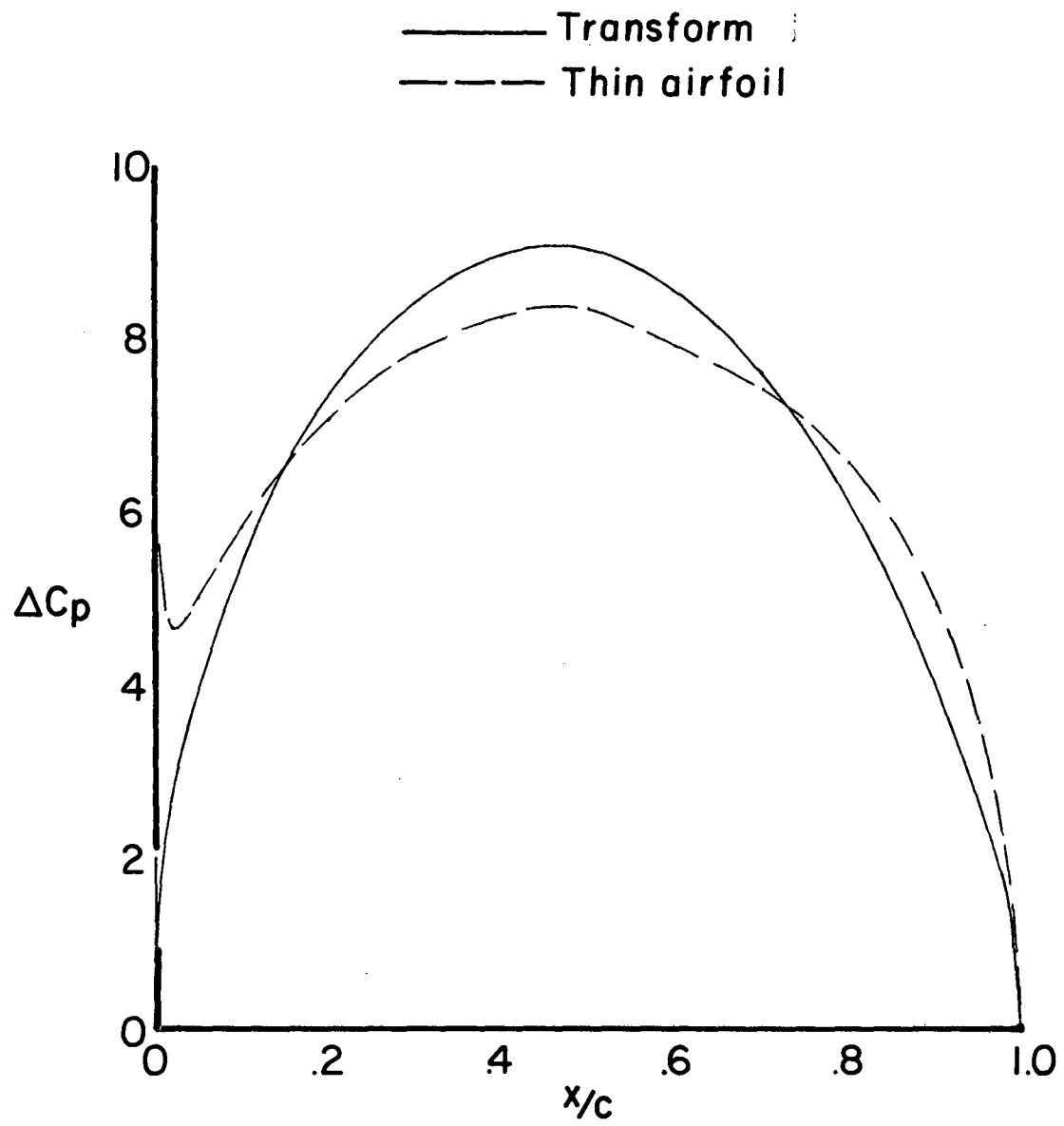


Figure 3. - Two-dimensional lifting pressure coefficient distribution
for $h/c = 0.5$ at $\alpha = 5^\circ$.

TABLE VI continued

Method	$h/c = .5$			
	$\alpha = 0^\circ$		$\alpha = 5^\circ$	
	c_l	x_{cp}	c_l	x_{cp}
Transform	6.2832	.50	6.8069	.4800
Thin airfoil	6.2832	.50	6.8315	.4799

Note, in particular, that the center-of-pressure predictions by both procedures yield the same results at both angles of attack; whereas, the thin airfoil theory predicts a higher lift than the transform method only at $\alpha = 5^\circ$. This relationship for the lift at $\alpha > 0^\circ$ between the solution on the surface (transform) and along the chord (thin airfoil) will be useful later.

Over an Aspect Ratio Range

The effects of aspect ratio on the center of pressure can be seen in figure 4 for both cambered and flat wings. It is interesting to note that for decreasing aspect ratio the predicted flat wing centers of pressure move forward as expected; whereas, for cambered wings at $\alpha = 0^\circ$ the centers of pressure progress rearward when computed by all three theoretical methods. A comparison of the curves shows that the present method and the modified Multhopp cambered-wing- x_{cp} results agree well and tend toward the two-dimensional limit. They both also show a more rearward location of x_{cp} at all aspect ratios

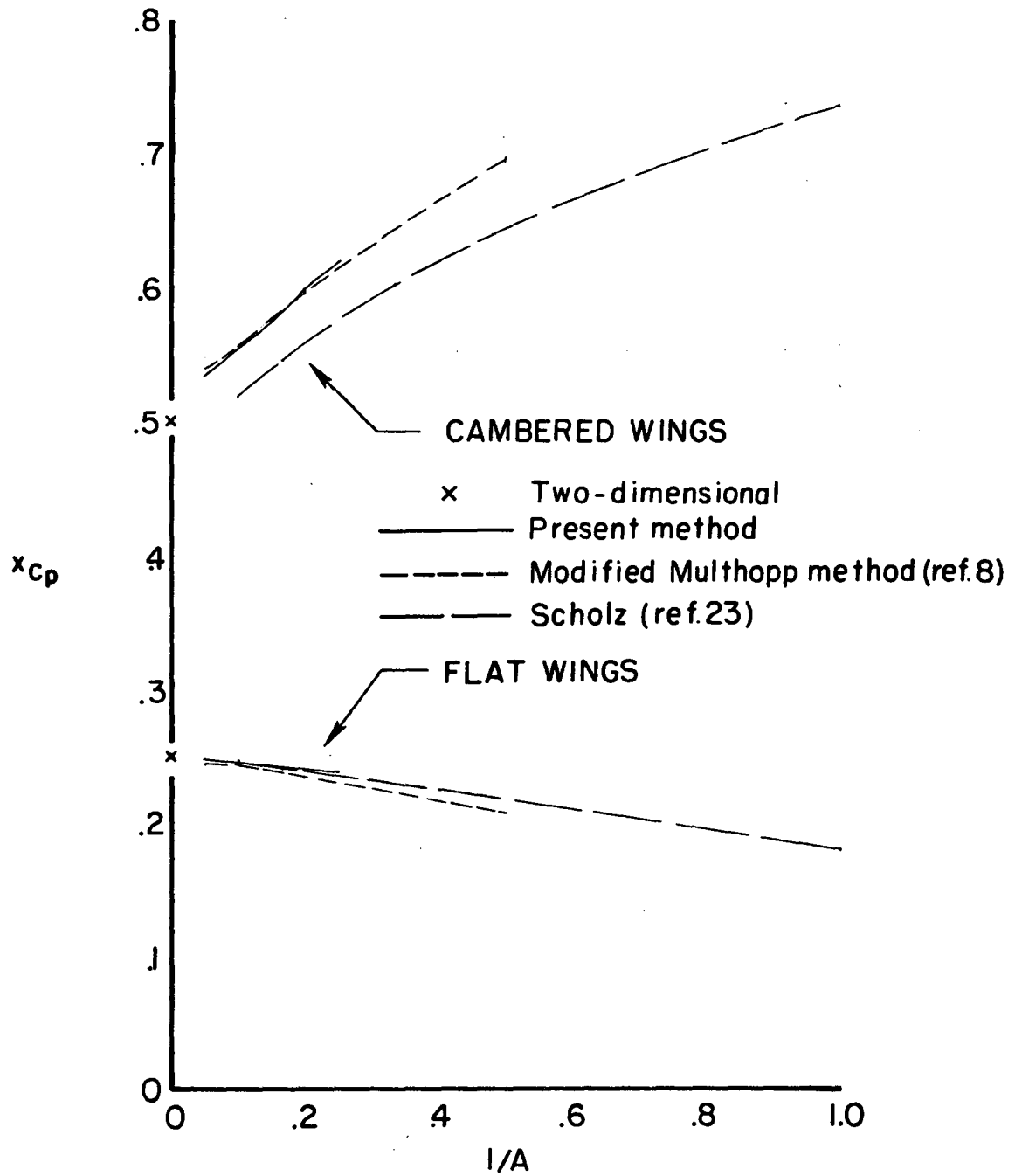
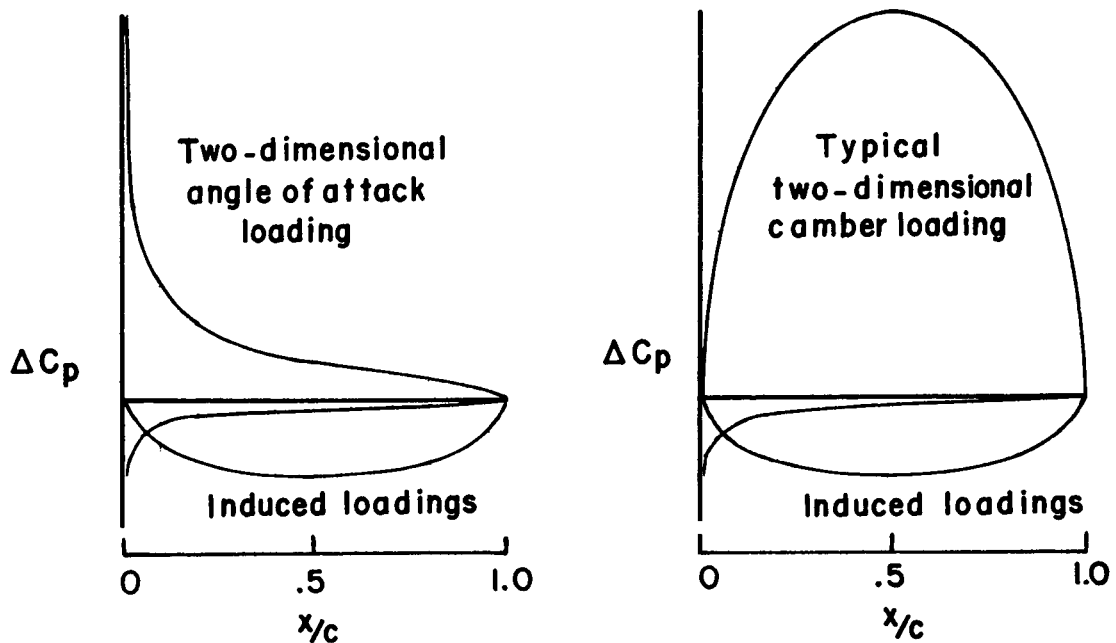


Figure 4. - Effect of camber on center of pressure. Cambered wing results are at $\alpha = 0^\circ$.

than those predicted by Scholz. For the flat wings the present method results tend toward the two-dimensional value of x_{cp} slightly faster than the other two methods with increasing aspect ratio. At $\alpha = 0^\circ$, the effect of camber cannot be seen at a given aspect ratio because the different camber curves tend to collapse upon one another. Hence, these effects are discussed in the next section at a given aspect ratio and positive angle of attack.



Sketch 9. Loading composition for finite-aspect ratio flat and cambered wings

The above center-of-pressure trends can best be understood by examining the preceding sketches. The effects of finite aspect ratio are seen to induce both a negative $\cot \epsilon/2$ load and a negative $\sin \epsilon$ load with these induced loads becoming larger as the aspect ratio decreases. For flat wings, the induced $\cot \epsilon/2$ load does not change the load

center but does decrease the lift at a given α ; however, not only does the $\sin \epsilon$ load decrease lift, it also imposes a nose-up moment about the two-dimensional lift center as well as the leading edge. These effects lead to a forward movement of the center of pressure with decreasing aspect ratio. For symmetrically cambered wings (in particular, circular-arc wings at $\alpha = 0^\circ$), the induced $\sin \epsilon$ load reduces the lift at a given α without disturbing the center of pressure; whereas the induced $\cot \epsilon/2$ load decreases the lift and produces a nose-up moment about the leading edge or a nose-down moment about the two-dimensional lift center. These two effects cause the center of pressure on cambered wings to move increasingly rearward with decreasing aspect ratio.

The trend of center of pressure with aspect ratio is well known for flat wings; however, the corresponding trend for cambered wings is not as well known, even though documented by Scholz in reference 23.

Over a Camber Ratio Range

The effects of camber ratio on x_{cp} and C_L are seen in figures 5(a) and 5(b), respectively, for an aspect ratio 5 rectangular wing at $\alpha = 5^\circ$. As expected, the predicted results show an increase in C_L and rearward movement of x_{cp} with increasing h/c . Furthermore, comparisons made between the modified Multhopp method and the present method indicate that the centers of pressure agree reasonably well up to h/c of .013; whereas, the C_L predicted by the present method exceed those of the modified Multhopp method for all camber and increases at a faster rate.

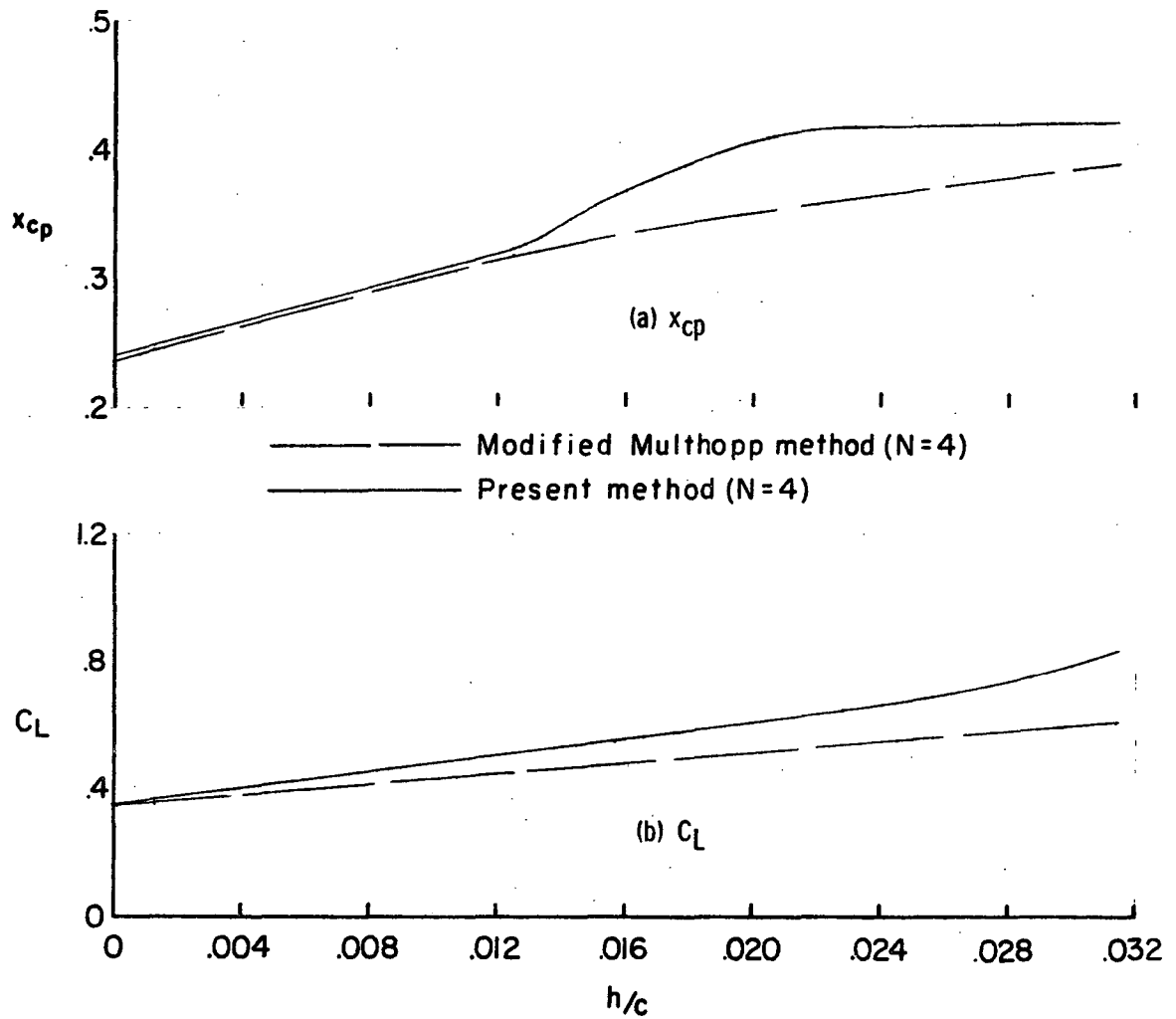


Figure 5. - Effect of camber on some aerodynamic characteristics of an $A = 5$ rectangular wing at $\alpha = 5^\circ$.

Over an Angle-of-Attack Range

The variation of C_L with α at an aspect ratio of 5 and camber ratio of 0.0314 are computed for both the modified Multhopp and present methods, and the results presented in figure 6. The curves show that the present method predicts a higher value of C_L at all angles of attack and yields a higher lift-curve slope.

Discussion

From the preceding studies of the present method and the subsequent applications, much has been learned:

(1) Number and Locations of Control Points

Two control points (loading functions) are sufficient to describe adequately the wing having only small amounts of camber ($h/c \leq 0.00125$), and the results with different locations indicate a low sensitivity to position. This happens because the first two lifting pressure functions are adequate to describe the pressure loading and also satisfy the tangent flow boundary condition all along the arc. For higher camber ratios, more than two control points are required to constrain the flow sufficiently to meet the solution criteria. The number and location of these control points depend upon wing aspect ratio, and angle of attack because of the few control points constraining the flow. Numerical studies indicate that two additional terms in the Birnbaum pressure loading series are still not adequate to describe the loading distribution for wings with cambers in excess of 1.25%; therefore, a larger number of terms are required.

———— Modified Multhopp method (N=4)
———— Present method (N=4)

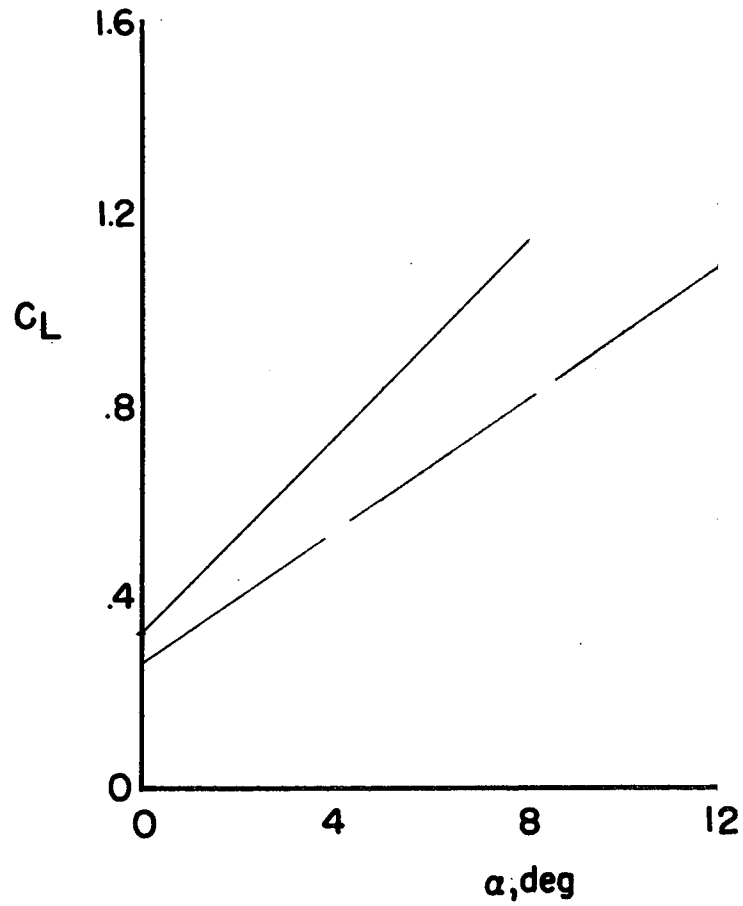


Figure 6. - Effect of angle of attack on C_L for an $A = 5$,
 $h/c = 0.0314$ rectangular wing.

This is not a very practical solution since it necessitates an excessive amount of computer time. For example, with two spanwise stations and four chordwise loading functions, computer time on the CDC 6600 of 15 minutes is required, and for six chordwise modes, time in excess of 30 minutes would be needed. Ideally then one would utilize a better set of modal functions. The problem is the determination of this better set. One procedure for doing this would be to obtain them from the local pressure equation given in appendix C for the exact two-dimensional solution. Another would be to obtain them from the two-dimensional integral equation relating the downwash ratio or local slope to the pressure distribution over Δx . Still a third procedure would be to express the series of loading functions in terms of distance along the arc having the appropriate singularity as the first term with the other terms having the first term multiplied by distance along the arc to a power.

The first procedure would be very difficult, as an examination of equations C-23 and C-24 will easily show. The second procedure leads to another series solution which is as yet undetermined. It is likely, however, that many terms would be required. The third procedure has been programmed, with only slight improvements obtained.

(2) Limiting Values

The present solution tends to the correct two-dimensional value of x_{cp} for both the flat wing and at $\alpha = 0^\circ$ for the cambered wing. The present method also predicts a C_L which tends to the two-dimensional value for $h/c \leq 0.0314$ and $\alpha = 5^\circ$. It is interesting to note that, whereas the two-dimensional solution along the chord (thin airfoil)

predicts a higher c_l than the solution along the surface (transform), the reverse is true for the two three-dimensional solutions at both $A = 20$ and $A = 5$.

(3) Moderate Aspect Ratio Comparison

The present method appears to predict reasonably well the aerodynamic characteristics of wings with small camber ($h/c \leq 0.0125$). This is demonstrated by comparison with the experiment and the modified Multhopp method. The fact that at $h/c = 0.0314$ the present method yields a higher C_L at any α , a higher C_{L_α} , and a more rearward x_{cp} than the modified Multhopp method can be attributed to both the modal functions employed in the present method and the limitations inherent in the planar approach. It should be noted that even with the modal functions employed satisfying the solution criteria, poor results can be obtained because of the limited number of terms used.

IX. CONCLUSIONS

The development of a nonplanar lifting surface method having a continuous distribution of singularities and satisfying the tangent flow boundary condition on the mean camber surface is given in this dissertation. The method predicts some incompressible longitudinal aerodynamic coefficients of rectangular wings which have circular-arc camber. After some preliminary sensitivity studies are conducted with this method, applications are made over an aspect- and camber-ratio and angle-of-attack range and the results compared herein with other theoretical methods and flat-wing experimental data. From these studies and comparisons, several conclusions emerge. They are: (1) The present method is able to predict with good accuracy some longitudinal aerodynamic characteristics for camber ratios not greater than 0.00125 at both high and moderate aspect ratio by employing only two control points (with little sensitivity of results to control point locations) and without the singular strip encountered in the flat-wing theoretical solutions. (2) For higher camber ratios, more control points are required, but even with their locations yielding results which give reasonable agreement between the far-field and near-field induced drag values (the solution criteria), the lifting pressure distributions can be poor. The poor distributions and high sensitivity of results to control point location indicate that the pressure mode functions chosen are not the most appropriate for wings having cambers in excess of 1.25%. Other lifting pressure functions were investigated without obtaining any significant improvement in the results. (3) The control point locations are

dependent upon aspect ratio (because of the few control points used), camber ratio, and angle of attack, because of the inadequacy of the modal functions chosen. (4) The present method is also able to predict reasonably well the lift coefficient and center of pressure for moderate aspect ratio (aspect ratio 5 illustrated) at an angle of attack of 5° up to a camber ratio of about 1.25% . (5) The present method's predictions at a moderate aspect ratio of lift coefficient at any angle of attack and lift-curve slope, as well as center of pressure, are larger than those of the modified Multhopp method for all camber ratios. The over-prediction of the lift coefficient by the present method when compared with the modified Multhopp method is the reverse of that found in comparison of the two-dimensional surface (transformed) and chordal (thin airfoil) solutions. This indicates that the modified Multhopp results are low for certain configurations and that for others the lifting pressure functions of the present method are not appropriate.

X. RECOMMENDATIONS

The work reported herein could serve as a model for lifting surface solutions of other basic camber shapes such as elliptic, parabolic, or those represented by some other general function. However, it should be kept in mind that each of these other camber shapes has a different set of appropriate chordal loading functions which must be determined in order to yield acceptable results in a reasonable amount of computer time. Another way to save computer time would be to perform the general spanwise integration analytically first, leaving only the chordwise integration to be done numerically.

Extensions to the present work could be undertaken to include both the effects of sweepback, without introducing reversed twist, and variable dihedral.

XI. REFERENCES

1. Prandtl, L.: Applications of Modern Hydrodynamics to Aeronautics. NACA TR 116, 1921.
2. Multhopp, Hans: The Calculation of the Lift Distribution of Aerofoils. RTP Translation 3292. Durand Reprinting Committee.
3. Mutterperl, William: The Calculation of Span-Load Distributions on Sweptback Wings. NACA TN 834, 1941.
4. Weissinger, J.: The Lift Distribution of Swept-Back Wings. NACA TN 1120, 1947.
5. Faulkner, V. M.: The Calculation of Aerodynamic Loading on Surfaces of Any Shape. R&M, 1910, 1943.
6. Multhopp, Hans: Methods for Calculating the Lift Distribution of Wings (Subsonic Lifting-Surface Theory). R&M 2884, Brit. A.R.C., 1950.
7. Van Spiegel, E.; and Wouters, J. G.: Modifications of Multhopp's Lifting-Surface Theory With a View to Automatic Computation. NLR - TN W.2, Nat. Lucht-Ruimtevaartlab (Amsterdam), 1962.
8. Lamar, John E.: A Modified Multhopp Approach for Predicting Lifting Pressures and Camber Shape for Composite Planforms in Subsonic Flow. NASA TN D-4427, 1968.
9. Wagner, Siegfried: On the Singularity Method of Subsonic Lifting-Surface Theory. AIAA Paper No. 69-37. Jan., 1969.
10. van de Vooren, A. I.: Some Modifications to Lifting-Surface Theory. Journal of Engineering Mathematics (Dutch), Vol. 1, No. 1, pp. 87-101, Jan., 1967.
11. Rupert, Paul E: Theoretical Characteristics of Arbitrary Wings by a Non-Planar Vortex Lattice Method. Doc. No. D6-9244, Boeing Co., Feb., 1964.
12. Belotserkovskii, S. M.: Special Features of Subsonic Flow Past Wings of Complex Plan-Form. Libr. Transl. 1297, British R.A.E., April, 1968.

13. Hedman, Sven G.: Vortex-Lattice Method for Calculation of Quasi Steady State Loadings on Thin Elastic Wings in Subsonic Flow. FFA Rep. 105, Aeronautical Research Institute of Sweden, 1966.
14. Margason, Richard J.: and Lamar, John E.: Vortex-Lattice Fortran Program for Estimating Subsonic Aerodynamic Characteristics of Complex Planforms. NASA TND-6142, 1971.
15. Vivian, H. T.; and Andrews, L. V.: Unsteady Aerodynamics for Advanced Configurations; Part I - Application of the Subsonic Kernel Function to Nonplanar Lifting Surfaces. FDL - TD12-64-152, May, 1965.
16. Rotta, Nicholas R.: The Non-Planar, Moderate Aspect Ratio, Subsonic Wing. Ph.D. Thesis. New York University, School of Engineering and Science, 1968.
17. Kalman, T. P.; Rodden, W. P.; and Giesing, J. P.: Application of the Doublet-Lattice Method to Nonplanar Configurations in Subsonic Flow. AIAA Paper No. 70-539, May, 1970.
18. Stark, V. J. E.: Aerodynamic Forces on a Combination of a Wing and a Fin Oscillating in Subsonic Flow. Report TN54, Saab Aircraft Company, Linköping, Sweden, 1964.
19. Nielson, J. N.; Spangler, S. B.; Stahara, S.S.; and Lee, A. L.: An Exploratory Aerodynamic and Structural Investigation of All Flexible Parawings. NASA CR-1674, December, 1970.
20. Ashley, Holt; and Landahl, Marten: Aerodynamics of Wings and Bodies. Addison-Wesley Publishing Co., Inc., Reading, Mass., 1965.
21. Peirce, B. O.: A Short Table of Integrals. Third Revised Edition, Ginn and Company, Boston, 1929.
22. Flachsbart, O.: Messungen an ebenen und gewölbten Platten. Ergebnisse der Aerodynamischen Versuchsanstalt zu Göttingen. Vol. IV, pp. 96-100, 1932.
23. Scholz, N.: Beiträge zur Theorie der Tragenden Fläche. Ing. Arch. Vol. 18, pp. 84-105, 1950.
24. Brebner, G. G.; Wyatt, L. A.; and Ilt, Gladys P.: Low-Speed Wind-Tunnel Test on a Series of Rectangular Wings of Varying Aspect Ratio and Aerofoil Section. C. P. 916, Brit. A.R.C., 1967.
25. Kuthe, A. M.; and Schetzer, J. D.: Foundations of Aerodynamics. Second Edition, John Wiley & Sons, Inc., New York, 1964.

26. Pope, Alan: Basic Wing and Airfoil Theory. First Edition, McGraw-Hill, New York, 1951.
27. Milne-Thompson, L. M.: Theoretical Aerodynamics. Second Edition, MacMillan & Co., Ltd., London, 1952.
28. Rauscher, Manfred: Introduction to Aeronautical Dynamics. John Wiley & Sons, Inc., New York, 1953.
29. Durand, William Frederick (Editor): Aerodynamic Theory. Vol. II. Div. E. Dover Publications, Inc., New York, 1963.

XII. VITA

The author was born in [REDACTED] and attended local elementary and high schools. He entered the University of Alabama in September, 1957, and completed the requirements for a Bachelor of Science degree in both Aerospace and Mechanical Engineering in January, 1962. At that time, he received a Research Assistantship and began his Master of Science program in Aerospace Engineering. He completed the requirements for that degree in February, 1963, and subsequently became an Aerospace Technologist with the NASA at the Langley Research Center. In September, 1963, he commenced his academic course work at Virginia Polytechnic Institute leading toward the present degree.

The author's major field of interest is the prediction of pressure distribution on lifting wings and wing-body combinations at subsonic speeds.

[REDACTED]

XIII. APPENDIX A

Certain Integrals Over The Box

Some of the integrals presented in equation (41) for integration over the box contain in the integrand the term $\left(\frac{1}{\sigma^2 \cos^2 \theta + (\omega/R)^2}\right)$. The solution for these definite integrals can be analytically formulated; however, obtaining correct results from the numerical evaluation of these formulations may be difficult. The difficulty is evident for θ near $\pi/2$, because there the numerical evaluation of the general formulation does not tend smoothly to the same numerical result as would be obtained by a direct integration of the original integrals for $\theta = \pi/2$. The numerical difficulty arises because of the general occurrence of $(1/\cos \theta)$ as an overall multiplier, as can be seen in the following example.

Example:

Consider the surface integration of

$$R \int_{-\bar{\sigma}}^{\bar{\sigma}} \int_{\frac{\bar{\omega}}{R}}^{\frac{\bar{\omega}}{R}} \frac{\sigma^2 d(\omega/R) d\sigma}{[\sigma^2 \cos^2 \theta + (\omega/R)^2]^2} \quad (\text{A-1})$$

Integrating expression (A-1) with respect to ω/R and imposing the limits leads to

$$\frac{R}{\cos^3 \theta} \left[\cos \theta \int_{-\bar{\sigma}}^{\bar{\sigma}} \frac{(\bar{\omega}/R) d\sigma}{\sigma^2 \cos^2 \theta + (\bar{\omega}/R)^2} + \int_{-\bar{\sigma}}^{\bar{\sigma}} \frac{\tan^{-1} \left(\frac{\bar{\omega}}{R \sigma \cos \theta} \right)}{\sigma} d\sigma \right] \quad (\text{A-2})$$

The first integral of expression (A-2) can be evaluated readily; however, a change of variable is needed in the second. These steps

lead to

$$\frac{R}{\cos^3 \theta} \left[2 \tan^{-1} \left(\frac{R\bar{\sigma} \cos \theta}{\bar{\omega}} \right) + \int_{\frac{-R\bar{\sigma} \cos \theta}{\bar{\omega}}}^{\frac{R\bar{\sigma} \cos \theta}{\bar{\omega}}} \frac{[\pi/2 - \tan^{-1}(x)]}{x} dx \right] \quad (\text{A-3a})$$

where

$$x = R\bar{\sigma} \cos \theta / \bar{\omega} \quad (\text{A-3b})$$

The first term in the remaining integral integrates to zero because it is odd over the integration range. The second term has to be integrated term by term after expanding $\tan^{-1}(x)$ into

$$\tan^{-1}(x) = x - \frac{x^3}{3} + \frac{x^5}{5} - \frac{x^7}{7} + \dots \quad (\text{A-4})$$

Hence, upon performing the above integrations and letting

$$R\bar{\sigma} = \bar{\omega} \quad (\text{A-5})$$

leads to

$$\frac{R}{\cos^3 \theta} \left[2 \tan^{-1}(\cos \theta) - 2 \left(\cos \theta - \frac{\cos^3 \theta}{9} + \frac{\cos^5 \theta}{25} - \frac{\cos^7 \theta}{49} + \dots \right) \right] \quad (\text{A-6})$$

This expression could be considered as the general formulation of the evaluated definite integral appearing in expression (A-1). Note that, in expression (A-6), values of θ near $\pi/2$ produce large results for the $(1/\cos^3 \theta)$ multiplier and small results for the terms inside the braces. Now, upon performing the indicated multiplications, there result some terms which are still small and tend to zero as θ goes to $\pi/2$; whereas, other products, $\frac{2R \tan^{-1}(\cos \theta)}{\cos^3 \theta}$ and $\frac{-2R \cos \theta}{\cos^3 \theta}$, produce numerical indeterminacies or, at best, infinities of opposite sign. In either case, the answer or finite part of the surface

integral is not determinable.

This problem can be circumvented by expanding in expression (A-6) the term $\tan^{-1}(\cos\theta)$ according to equation (A-4) and combining like terms inside the braces. After simplifying, the result is

$$R \left(-\frac{4}{9} + \frac{8}{25} \cos^2\theta - \frac{12}{49} \cos^4\theta + \dots \right) \quad (\text{A-7})$$

Now, for $\theta = \pi/2$, the expression, instead of producing indeterminacies, gives a value of $-\frac{4}{9} R$. This result agrees with the direct integration of expression (A-1) for $\theta = \pi/2$.

Another integral which must be integrated in the same manner as the preceding is

$$R \int_{-\bar{\sigma}}^{\bar{\sigma}} \int_{-(\bar{\omega}/R)}^{(\bar{\omega}/R)} \frac{d(\omega/R) d\sigma}{\sigma^2 \cos^2\theta + (\omega/R)^2} \quad (\text{A-8})$$

and results in

$$-4R \left(1 - \frac{1}{9} \cos^2\theta + \frac{1}{25} \cos^4\theta \dots \right) \quad (\text{A-9})$$

XIV. APPENDIX B

Determination of Aerodynamic Coefficients

The determination of some section and wing aerodynamic coefficients for wings with circular-arc camber is accomplished by using the c_{nm} set computed from equation (46) and the equations given in the following paragraphs.

Section Coefficients

The computational equations for the section lift (including the contribution due to leading-edge suction) pitching moment, distributed camber drag and leading-edge suction coefficients are given below.

Section lift coefficient:

$$c_l(y_j) = \frac{1}{\pi} \sum_{\substack{m=0 \\ \text{even}}}^2 \left[\sum_{n=0}^{N-1} c_{nm} \int_0^\pi \frac{h_n(\epsilon) \sin \vartheta \sin \epsilon d\epsilon}{\sin(\vartheta + \alpha)} + \frac{c_{0m}^2}{2\pi} \frac{\cos \theta_0}{\sin^2 \theta_0 \sin(\theta_0 + \alpha)} \right] \left(\frac{y_j}{b/2} \right)^m \sqrt{1 - \left(\frac{y_j}{b/2} \right)^2} \quad (\text{B-1})$$

Section pitching-moment coefficient:

$$c_{m_{LE}}(y_j) = \frac{1}{\pi} \frac{R}{c} \sum_{\substack{m=0 \\ \text{even}}}^2 \sum_{n=0}^{N-1} c_{nm} \int_0^\pi \frac{h_n(\epsilon) \sin(\vartheta - \theta_0) \sin \epsilon d\epsilon}{\sin(\vartheta + \alpha)} \left(\frac{y_j}{b/2} \right)^m \sqrt{1 - \left(\frac{y_j}{b/2} \right)^2} \quad (\text{B-2})$$

Section distributed camber drag coefficient:

$$c_{d_c}(y_j) = \frac{1}{\pi} \sum_{\substack{m=0 \\ \text{even}}}^2 \sum_{n=0}^{N-1} c_{nm} \int_0^\pi \frac{h_n(\epsilon) \cos \vartheta \sin \epsilon d\epsilon}{\sin(\vartheta + \alpha)} \left(\frac{y_j}{b/2} \right)^m \sqrt{1 - \left(\frac{y_j}{b/2} \right)^2} \quad (\text{B-3})$$

Section leading-edge suction coefficient:

$$c_{s_{LE}}(y_j) = \sum_{\substack{m=0 \\ \text{even}}}^2 \frac{c_{om}^2}{2\pi} \frac{1}{\sin^2 \theta_o \sin(\theta_o + \alpha)} \left(\frac{y_j}{b/2}\right)^m \sqrt{1 - \left(\frac{y_j}{b/2}\right)^2} \quad (B-4)$$

where

$$\vartheta = \cos^{-1} \left[\frac{(1 - \cos \epsilon)}{2} \frac{c}{R} + \cos(\theta_o + \alpha) \right] - \alpha \quad (B-5)$$

Wing Coefficients

The equations used to determine the wing lift, pitching moment, distributed camber drag, leading-edge suction and near-field induced-drag coefficients were determined by Multhopp quadrature and are given as follows for symmetrical span loadings.

Wing lift coefficient:

$$C_L = \frac{\pi}{c_{av}(J+1)} \left(\sum_{j=1}^{\frac{J-1}{2}} c_l(y_j) c(y_j) \sin \phi_j + \frac{1}{2} c_l\left(\frac{y_{J+1}}{2}\right) c\left(\frac{y_{J+1}}{2}\right) \right) \quad (B-6)$$

Wing pitching-moment coefficient:

$$C_{m_{LE}} = \frac{\pi}{c_{av} c_{ref}(J+1)} \left(\sum_{j=1}^{\frac{J-1}{2}} c_{m_{LE}}(y_j) c^2(y_j) \sin \phi_j + \frac{1}{2} c_{m_{LE}}\left(\frac{y_{J+1}}{2}\right) c^2\left(\frac{y_{J+1}}{2}\right) \right) \quad (B-7)$$

Wing distributed camber drag coefficient:

$$C_{D_c} = \frac{\pi}{c_{av}(J+1)} \left(\sum_{j=1}^{\frac{J-1}{2}} c_{d_c}(y_j) c(y_j) \sin \phi_j + \frac{1}{2} c_{d_c}\left(\frac{y_{J+1}}{2}\right) c\left(\frac{y_{J+1}}{2}\right) \right) \quad (B-8)$$

Wing leading-edge suction coefficient:

$$C_{s_{LE}} = \frac{\pi}{c_{av}(J+1)} \left(\sum_{j=1}^{\frac{J-1}{2}} c_{s_{LE}}(y_j) c(y_j) \sin \phi_j + \frac{1}{2} c_{s_{LE}}\left(\frac{y_{J+1}}{2}\right) c\left(\frac{y_{J+1}}{2}\right) \right) \quad (B-9)$$

Wing near-field induced-drag coefficient:

$$C_{D_{ii}} = C_{D_c} - C_{s_{LE}} \sin \theta_o \quad (B-10)$$

where

$$\phi_j = \frac{j\pi}{J+1} \quad (B-11)$$

Wing far-field induced-drag coefficients:

$$C_{D_i} = A \int_{-1}^1 \frac{c_1 c}{2b} \alpha_i d\eta \quad (B-12)$$

XV. APPENDIX C

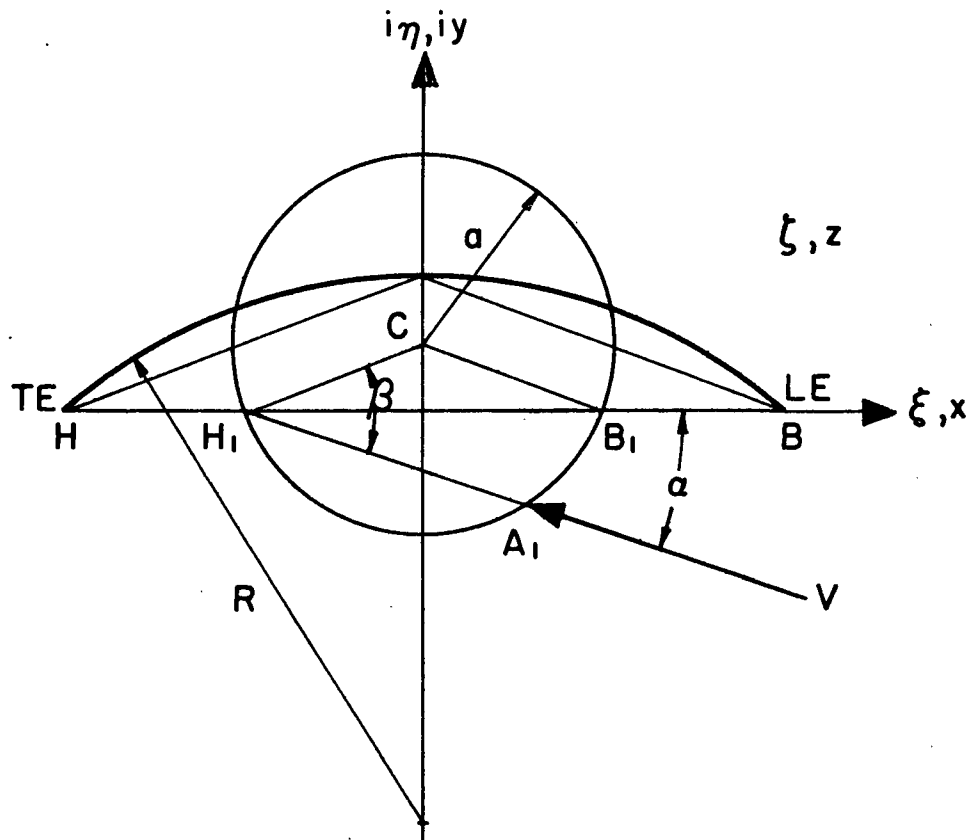
Two-Dimensional Circular-Arc Airfoil

Aerodynamic Characteristics

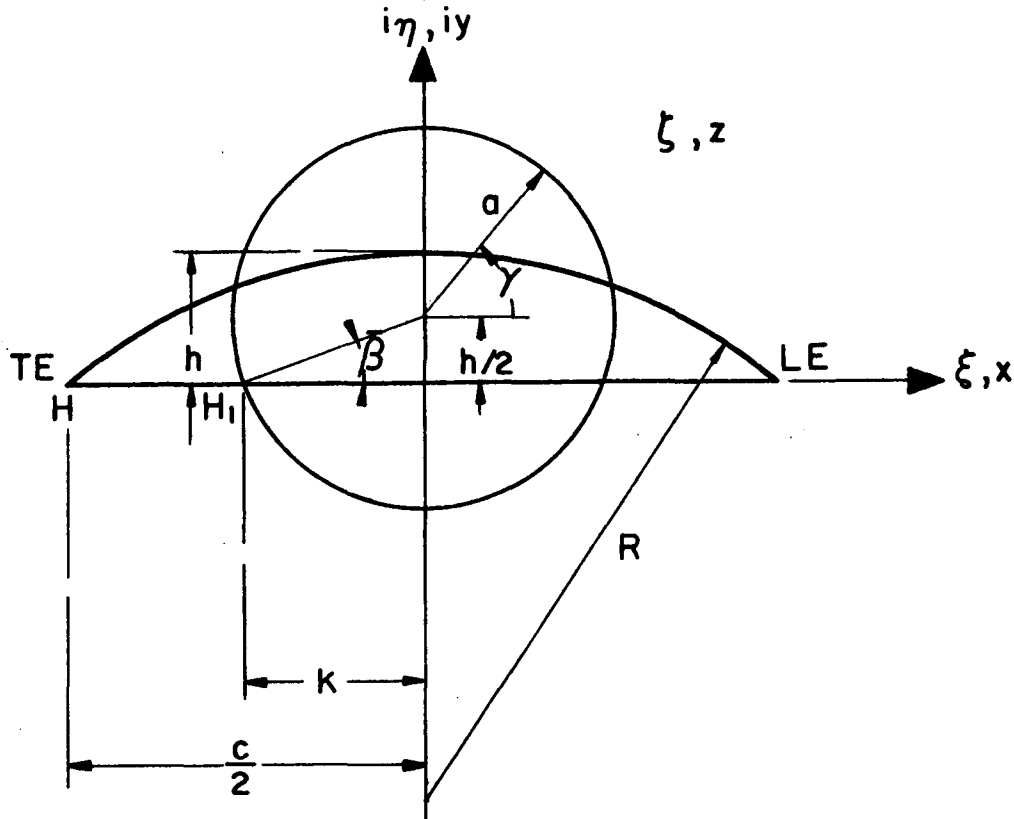
It is well known (see refs. 26 to 29) that a circle in the complex ζ -plane can be mapped into a circular-arc airfoil in the complex z -plane by selecting the origin of the circle to lie at $ih/2$ and then applying the Kutta-Joukowski transform

$$z = \zeta + \frac{k^2}{\zeta} \quad (C-1)$$

to points on the perimeter of the circle (see sketches 10 and 11). The



Sketch 10.- Geometrical relationships between generating circle and circular-arc airfoil.



Sketch 11.- Additional geometrical relationships between generating circle and circular-arc airfoil.

points from B_1 counterclockwise to H_1 will lie on the upper surface and those from H_1 counterclockwise to B_1 will lie on the lower surface. The local velocity, and hence pressure, can be determined over the airfoil by making use of the complex potential (w) of the circle of an angle of attack and the Kutta-Joukowski transformation as follows:

$$u - iv = - \frac{dw}{dz} = - \frac{dw}{d\zeta} \frac{d\zeta}{dz} \quad (C-2)$$

where

$$w = V\zeta e^{i\alpha} + \frac{Va^2 e^{-i\alpha}}{\zeta - s} + 2aiV\sin\beta \ln(\zeta - s) \quad (C-3)$$

- s location of the center of the circle in ζ -plane
- β the angle $\angle CH_1A_1$, where H_1 is the point on the circle that transforms into the trailing edge of the airfoil (point H).

The angle β must be such that the velocity at the point H remains finite. To solve for the required β relationship, the procedure given in reference 26 will be followed. Begin with

$$\frac{dw}{d\zeta} = Ve^{i\alpha} - \frac{Va^2e^{-i\alpha}}{(\zeta - s)^2} + \frac{2aiV\sin\beta}{\zeta - s} \quad (C-4a)$$

or re-express it as

$$\frac{dw}{d\zeta} = v \left(e^{i\alpha} + \frac{ae^{i\beta}}{\zeta - s} \right) \left(1 - \frac{ae^{-i(\alpha + \beta)}}{\zeta - s} \right) \quad (C-4b)$$

and the differential of equation (C-1)

$$\frac{d\zeta}{dz} = \frac{\zeta^2}{\zeta^2 - k^2} \quad (C-5)$$

Upon substituting equations (C-4b) and (C-5) into (C-2), it follows that

$$\frac{dw}{dz} = v \left(e^{i\alpha} + \frac{ae^{i\beta}}{\zeta - s} \right) \left(1 - \frac{ae^{-i(\alpha + \beta)}}{\zeta - s} \right) \left(\frac{\zeta^2}{\zeta^2 - k^2} \right) \quad (C-6)$$

The point H_1 on the circle can be seen in sketch 11 (ref. 27) and corresponds to $\zeta = -k$. In order to keep the velocity from taking on an infinite value at the transformed point H, the point H_1 must be made a stagnation point ($dw/d\zeta = 0$) so that dw/dz will assume

the indeterminant form of $0/0$, which can be shown to yield a finite velocity at the trailing edge.

Next, the angle β must be related to other known quantities. This is accomplished by examining the geometry of the generating circle in sketch 11. From it the distance along ξ from H_1 to the horizontal projection of the circle center is determined to be

$$k + s_\xi = a \cos(\beta - \alpha) + 0 = a \cos \bar{\beta} \quad (C-7a)$$

Furthermore, the vertical distance along η is found to be

$$s_\eta = a \sin(\beta - \alpha) = a \sin \bar{\beta} \quad (C-7b)$$

These can be written as

$$k + is_\eta = a [\cos(\beta - \alpha) + i \sin(\beta - \alpha)] = ae^{i(\beta - \alpha)} \quad (C-8a)$$

or

$$ae^{i\beta} = (k + s) e^{i\alpha} \quad (C-8b)$$

By making use of equation (C-8b) in the first group of terms in equation (C-6), the following result can be obtained:

$$\frac{dw}{dz} = v \left(e^{i\alpha} + \frac{(k + s)e^{i\alpha}}{\zeta - s} \right) \left(1 - \frac{ae^{-i(\alpha + \beta)}}{\zeta - s} \right) \frac{\zeta^2}{(\zeta - k)(\zeta + k)} \quad (C-9)$$

which after some simplification can also be given as

$$\frac{dw}{dz} = ve^{i\alpha} \left[(\zeta - s) - ae^{-i(\alpha + \beta)} \right] \frac{\zeta^2}{(\zeta - s)^2(\zeta - k)} \quad (C-10)$$

With the addition and subtraction of k to the bracketed term, and upon using the result of equation (C-8b), equation (C-10) can be recast as

$$\frac{dw}{dz} = Ve^{i\alpha} \left(\zeta + k - ae^{i(\beta - \alpha)} - ae^{-i(\alpha + \beta)} \right) \frac{\zeta^2}{(\zeta - s)^2(\zeta - k)} \quad (C-11)$$

By expanding the exponent terms, equation (C-11) becomes

$$\frac{dw}{dz} = Ve^{i\alpha} \left(\zeta + k - 2ae^{-i\alpha} \cos\beta \right) \frac{\zeta^2}{(\zeta - s)^2(\zeta - k)} \quad (C-12)$$

An examination of the velocity at the point H (or where $\zeta = -k$) yields

$$u_H - iv_H = - \frac{dw}{dz} = Ve^{i\alpha} (0 - e^{-i\alpha} \cos\beta) \frac{k}{ae^{i2(\beta - \alpha)}} \quad (C-13)$$

or

$$u_H - iv_H = - \frac{V k \cos\beta}{ae^{i(2\beta - 2\alpha)}} \quad (C-14)$$

In order to obtain the conjugate of $u_H - iv_H$ the angle $2\beta - 2\alpha$ can be rotated π radians. That is

$$u_H + iv_H = - \frac{V k \cos\beta}{a} e^{i(2\beta - 2\alpha + \pi)} \quad (C-15)$$

Hence, if the angle that a tangent to the cusp at the trailing edge makes with the x -axis is $2\beta - 2\alpha$, finite velocities are obtained.

From sketch 11, it can be seen that

$$a^2 = k^2 \sec^2 \bar{\beta} \quad (C-16)$$

and

$$k = c/4 \quad (C-17)$$

When these are used in combination with equation (C-8b), the following can be written:

$$\frac{c}{4} \sec \bar{\beta} e^{i\beta} = \left(\frac{c}{4} + \frac{ih}{2} \right) e^{i\alpha} \quad (C-18a)$$

Therefore,

$$e^{i\beta} = \left(\frac{\frac{c}{4} + \frac{ih}{2}}{\frac{c}{4} \sec \bar{\beta}} \right) e^{i\alpha} \quad (C-18b)$$

Taking the natural log of both sides leads to

$$i\beta = \ln \left(\cos \bar{\beta} + \frac{i2h}{c} \cos \bar{\beta} \right) + i\alpha \quad (C-19a)$$

or

$$i\beta = \frac{\ln \left(\cos^2 \bar{\beta} + \frac{4h^2}{c^2} \cos^2 \bar{\beta} \right)}{2} + i \tan^{-1} \left(\frac{2h}{c} \right) + i\alpha \quad (C-19b)$$

which yields

$$\beta = \tan^{-1} \left(\frac{2h}{c} \right) + \alpha = \bar{\beta} + \alpha \quad (C-20)$$

In order to determine the pressures on the airfoil, it is more convenient to specify locations on the circle and then determine the corresponding point on the airfoil rather than conversely. Hence, by defining

$$\zeta \equiv ae^{i\gamma} + \frac{ih}{2} \quad (C-21)$$

and by substituting this along with equations (C-16), (C-17) and (C-20) into equation (C-12), the following equation can be written:

$$\begin{aligned} \frac{dw}{dz} = & Ve^{i\alpha} \left(ae^{i\gamma} + \frac{ih}{2} + \frac{c}{4} - \frac{2k}{\cos\beta} e^{-i\alpha} \cos(\bar{\beta} + \alpha) \right) \cdot \\ & \cdot \frac{\left(ae^{i\gamma} + \frac{ih}{2} \right)^2}{\left(ae^{i\gamma} \right)^2 \left(ae^{i\gamma} + \frac{ih}{2} - \frac{c}{4} \right)} \end{aligned} \quad (C-22)$$

After all the multiplications and simplifications have been carried out, the velocities are determined from

$$u - iv = - \frac{dw}{dz} = - \frac{V \cos \bar{\beta} \left\{ \left[\cos \alpha P_1 - \sin \alpha P_2 \right] + i \left[\cos \alpha P_2 + \sin \alpha P_1 \right] \right\}}{\left(\frac{c}{2} \right) \left[1 - \cos(\gamma - \bar{\beta}) \right]} \quad (C-23)$$

where

$$\begin{aligned} P_1 = & -a \cos(\gamma + \bar{\beta}) + \left[a - \omega_R \cos \bar{\beta} + h \sin \bar{\beta} + \omega_I \sin \bar{\beta} \right] \\ & + \cos \gamma \left[\omega_R + \frac{h^2}{4a} \cos \bar{\beta} + \frac{h \omega_R \sin \bar{\beta}}{a} + \frac{h \omega_I}{a} \cos \bar{\beta} \right] \\ & + \sin \gamma \left[\omega_I + \frac{h \omega_I}{a} \sin \bar{\beta} + h + \frac{h^2}{4a} \sin \bar{\beta} - \frac{h \omega_R}{a} \cos \bar{\beta} \right] \\ & + \cos^2 \gamma \left[-\frac{h^2}{4a} + \frac{\omega_R h^2}{4a^2} \cos \bar{\beta} - \frac{h \omega_I}{a} - \frac{h^2 \omega_I}{4a^2} \sin \bar{\beta} \right] \\ & + \sin 2\gamma \left[\frac{h^2 \omega_I}{4a^2} \cos \bar{\beta} + \frac{h \omega_R}{a} + \frac{h^2 \omega_R}{4a^2} \sin \bar{\beta} \right] \\ & + \cos 3\gamma \left[-\frac{h^2 \omega_R}{4a^2} \right] + \sin 3\gamma \left[-\frac{h^2 \omega_I}{4a^2} \right] \end{aligned} \quad (C-23a)$$

$$\begin{aligned}
P_2 = & -a \sin(\gamma + \bar{\beta}) + [-\omega_I \cos \bar{\beta} - h \cos \bar{\beta} - \omega_R \sin \bar{\beta}] \\
& + \cos \gamma \left[\omega_I + \frac{h \omega_I}{a} \sin \bar{\beta} + h + \frac{h^2}{4a} \sin \bar{\beta} - \frac{h \omega_R \cos \bar{\beta}}{a} \right] \\
& - \sin \gamma \left[\omega_R + \frac{h^2}{4a} \cos \bar{\beta} + \frac{h \omega_R}{a} \sin \bar{\beta} + \frac{h \omega_I}{a} \cos \bar{\beta} \right] \\
& + \cos 2\gamma \left[\frac{h^2 \omega_I}{4a^2} \cos \bar{\beta} + \frac{h \omega_R}{a} + \frac{h^2 \omega_R}{4a^2} \sin \bar{\beta} \right] \\
& - \sin 2\gamma \left[-\frac{h^2}{4a} + \frac{h \omega_R}{4a^2} \cos \bar{\beta} - \frac{h \omega_I}{a} - \frac{h^2 \omega_I}{4a^2} \sin \bar{\beta} \right] \\
& + \cos 3\gamma \left[-\frac{h^2 \omega_I}{4a^2} \right] - \sin 3\gamma \left[-\frac{h^2 \omega_R}{4a^2} \right]
\end{aligned} \tag{C-23b}$$

and

$$\omega_R = -\frac{c}{2} \sec \bar{\beta} \cos \alpha \cos(\bar{\beta} + \alpha) + \frac{c}{4} \tag{C-23c}$$

$$\omega_I = \frac{h}{2} + \frac{c}{2} \sec \bar{\beta} \sin \alpha \cos(\bar{\beta} + \alpha) \tag{C-23d}$$

Hence

$$C_{p_{\text{local}}} = \frac{p - p_\infty}{\frac{1}{2} \rho V^2} \equiv 1 - \frac{[u^2 + v^2]}{V^2} \tag{C-24a}$$

$$= 1 - \frac{\cos^2 \bar{\beta} [P_1^2 + P_2^2]}{\left(\frac{c}{2}\right)^2 [1 - \cos(\gamma + \bar{\beta})]^2} \tag{C-24b}$$

The location on the airfoil which corresponds to the points on the circle at which the velocities are determined can be computed by substituting equation (C-21) into equation (C-1) and simplifying the resulting

expression. The result is

$$z = \frac{c}{4} \left[\left(\sec \bar{\beta} \cos \gamma + \frac{\cos \bar{\beta} \cos \alpha}{1 + 2 \sin \gamma \sin \bar{\beta} + \sin^2 \bar{\beta}} \right) + i \left(\sec \bar{\beta} \sin \gamma + \tan \bar{\beta} - \frac{\cos \bar{\beta} (\sin \gamma + \sin \bar{\beta})}{1 + 2 \sin \gamma \sin \bar{\beta} + \sin^2 \bar{\beta}} \right) \right] \quad (C-25)$$

These equations have been programmed and the lifting pressure results are compared with the three-dimensional solution at the mid-span of a rectangular wing with a very large aspect ratio in the Results and Discussion chapter of the dissertation.

The forces and pitching moment which are developed over the circular arc airfoil can be determined by direct integration of the pressures and the moment of the pressure over the airfoil or by employing the analogous integrations which result from Blasius' theorems. The Blasius' Theorem for forces (ref. 26) can be expressed as

$$X - iY = \frac{1}{2} i \rho \oint \left(\frac{dw}{dz} \right)^2 dz \quad (C-26)$$

or,

$$X - iY = - \frac{i \rho}{2} \oint \left(\frac{dw}{d\zeta} \right)^2 \left(\frac{d\zeta}{dz} \right) d\zeta \quad (C-27a)$$

By using equations (C-4b) and (C-5), equation (C-27a) can be written as

$$X - iY = - \frac{i \rho V^2}{2} \oint \left[(\zeta - s) e^{i\alpha} + a e^{i\beta} \right]^2 \cdot \left[(\zeta - s) - a e^{-i(\alpha + \beta)} \right]^2 \frac{\zeta^2 d\zeta}{(\zeta - s)^4 (\zeta^2 - k^2)} \quad (C-27b)$$

After expanding all of the terms and employing the Residue Theorem, the result is

$$X - iY = -i8\pi q a \sin\beta e^{i\alpha} \quad (C-28)$$

Hence

$$X = q 8\pi a \sin\beta \sin\alpha \quad (C-29a)$$

and

$$Y = q 8\pi a \sin\beta \cos\alpha \quad (C-29b)$$

With the substitutions for a , equation (C-16), and β , equation (C-20), the coefficients of forces in the x and y directions can be written as

$$c_x = 2\pi(\sin\bar{\beta} \cos\alpha + \cos\bar{\beta} \sin\alpha) \sec\bar{\beta} \sin\alpha \quad (C-30a)$$

or

$$c_x = 2\pi \left[\sin^2\alpha + \sin\alpha \cos\alpha \left(\frac{2h}{c} \right) \right] \quad (C-30b)$$

and

$$c_y = 2\pi(\sin\bar{\beta} \cos\alpha + \cos\bar{\beta} \sin\alpha) \sec\bar{\beta} \cos\alpha \quad (C-30c)$$

or

$$c_y = 2\pi \left[\sin\alpha \cos\alpha + \cos^2\alpha \left(\frac{2h}{c} \right) \right] \quad (C-30d)$$

Since

$$c_l = c_x \sin\alpha + c_y \cos\alpha \quad (C-31)$$

The resulting equation obtained by substituting in for c_x and c_y the equations (C-30b) and (C-30d), respectively, is

$$c_l = 2\pi \left[\sin\alpha + \cos\alpha \left(\frac{2h}{c} \right) \right] \quad (C-32a)$$

Also,

$$c_d = c_x \cos \alpha - c_y \sin \alpha \quad (C-32b)$$

and for the same substitutions as before leads to

$$c_d = 0 \quad (C-32c)$$

The Blasius Theorem for pitching moment from reference 26 about the center of the generating circle is simply

$$M_c = R \left[-\frac{1}{2} \rho \oint (z - z_c) \left(\frac{dw}{dz} \right)^2 dz \right] \quad (C-33a)$$

After substituting in it the results of equation (C-1) and sketch 11, this equation becomes

$$M_c = R \left[-\frac{1}{2} \rho \oint \left(\zeta + \frac{k^2}{\zeta} - \frac{ih}{2} \right) \left(\frac{dw}{d\zeta} \right)^2 \left(\frac{d\zeta}{dz} \right) d\zeta \right] \quad (C-33b)$$

and with the inclusion of the results of equations (C-4b) and (C-5), equation (C-33b) can be written as

$$M_c = R \left[-\frac{1}{2} \rho V^2 \oint \left[\frac{\zeta^2 + k^2}{\zeta} - \frac{ih}{2} \right] \left[(\zeta - s)e^{i\alpha} + ae^{i\beta} \right]^2 \cdot \right. \\ \left. \cdot \left[(\zeta - s) - ae^{-i(\alpha - \beta)} \right]^2 \frac{\zeta^2 d\zeta}{(\zeta - s)^4 (\zeta^2 - k^2)} \right] \quad (C-33c)$$

Upon expanding these terms, combining, simplifying and integrating each set of terms by the Residue Theorem, the following equation results:

$$M_c = q \pi \frac{c^2}{4} \sin 2\alpha \quad (C-34a)$$

or

$$c_{M_c} = \frac{\pi}{4} \sin 2\alpha \quad (C-34b)$$

After expressing α in a manner similar to reference 28, that is,

$$\alpha = \bar{\beta} + (\alpha - \bar{\beta}) \quad (C-35)$$

making use of the identity that

$$\sin 2\alpha = \sin 2[\bar{\beta} + (\alpha - \bar{\beta})] = -\sin 2\bar{\beta} + 2\cos(\alpha - \bar{\beta})\sin(\alpha + \bar{\beta}) \quad (C-36)$$

and re-expressing (C-32a) in terms of $\bar{\beta}$,

$$c_1 = 2\pi \sec \bar{\beta} [\sin(\alpha + \bar{\beta})] \quad (C-37a)$$

or

$$\sin(\alpha + \bar{\beta}) = \frac{c_1 \cos \bar{\beta}}{2\pi}, \quad (C-37b)$$

equation (C-34b) can be rewritten as

$$c_{M_c} = \frac{\pi}{4} \left[-\sin 2\bar{\beta} + \frac{2\cos(\alpha - \bar{\beta})c_1 \cos \bar{\beta}}{2\pi} \right] \quad (C-38a)$$

or

$$c_{M_c} = -\frac{\pi}{4} \sin 2\bar{\beta} + \frac{c_1}{4} \cos \bar{\beta} \cos(\alpha - \bar{\beta}) \quad (C-38b)$$

The first term is split off and defined by

$$c_{M_F} = -\frac{\pi}{4} \sin 2\bar{\beta}, \quad (C-39)$$

which is the pitching moment about the focus and is independent of α . The pitching-moment coefficient about the leading edge is obtained by transferring the moment about the center of the circle to the leading edge. Hence

$$c_{M_{LE}} = \frac{\pi}{4} \sin 2\alpha - 2\pi \left[\sin \alpha + \cos \alpha \left(\frac{2h}{c} \right) \right] \left(\frac{c}{2} \right) \quad (C-40a)$$

or

$$c_{M_{LE}} = \pi \left[\frac{\sin \alpha \cos \alpha}{2} - \sin \alpha - \cos \alpha \left(\frac{2h}{c} \right) \right] \quad (C-40b)$$

As a consequence of equation (C-40b) and equation (C-32a), x_{cp} can be written as

$$x_{cp} = \frac{\frac{\sin \alpha \cos \alpha}{2} - \sin \alpha - \cos \alpha \left(\frac{2h}{c} \right)}{-2 \left[\sin \alpha + \cos \alpha \left(\frac{2h}{c} \right) \right]} \quad (C-41)$$

These equations have also been programmed and results are compared with the three-dimensional solution in its limit in the Results and Discussion chapter of the dissertation.